Czech Technical University in Prague
Faculty of Nuclear Sciences and Physical Engineering
Department of Physics

Performance studies of the Muon Forward Tracker for ALICE upgrade

Master's thesis

Bc. Diana Mária Krupová

Supervisor: prof. Jesús Guillermo Contreras Nuño, PhD.

Praha, 2021

České vysoké učení technické v Praze
Fakulta jaderná a fyzikálně inženýrská
Katedra fyziky

Studium vlastností detektoru Muon Forward Tracker pro upgrade experimentu ALICE

Diplomová práce

Bc. Diana Mária Krupová

Vedoucí práce: prof. Jesús Guillermo Contreras Nuño, PhD.

Praha, 2021

ČESKÉ VYSOKÉ UČENÍ TECHNICKÉ V PRAZE
FAKULTA JADERNÁ A FYZIKÁLNĚ INŽENÝRSKÁ
PRAHA 1 - STARÉ MĚSTO, BŘEHOVÁ 7 - PSČ 115 19

Katedra: fyziky *Akademický rok:* 2020/2021

ZADÁNÍ DIPLOMOVÉ PRÁCE

Student: Bc. Diana Mária Krupová

Studijní program: Aplikace přírodních věd

Obor: Experimentální jaderná a částicová fyzika

Název práce: (česky) Studium vlastností detektoru Muon Forward Tracker pro upgrade ALICE

Název práce: (anglicky) Performance studies of the Muon Forward Tracker for ALICE upgrade

Pokyny pro vypracování:

1) Vypracování rešerše na téma: využití detektoru MFT ke zkoumání těžkých vůní a charmonií
2) Studium vlastností detektoru MFT pro měření fotoprodukce rho mezonu
3) Kalibrace sestaveného detektoru a charakterizace jeho pixelových senzorů

Doporučená literatura:

[1] G. Lutz: Semiconductor Radiation Detectors, Springer 2007

[2] ALICE Collaboration: Upgrade of the ALICE Experiment:Letter of Intent, J.Phys. G41 (2014) 087001

[3] ALICE Collaboration: Technical Design Report for the Muon Forward Tracker, https://cds.cern.ch/record/1981898

Jméno a pracoviště vedoucího diplomové práce:

prof. Jesús Guillermo Contreras Nuño, Ph.D.
Katedra fyziky, Fakulta jaderná a fyzikálně inženýrská ČVUT v Praze

Datum zadání diplomové práce: 23.10.2020

Termín odevzdání diplomové práce: 03.05.2021

Doba platnosti zadání je dva roky od data zadání.

.....
garant oboru

.....
vedoucí katedry

ČESKÉ VYSOKÉ UČENÍ TECHNICKÉ V PRAZE
Fakulta jaderná a fyzikálně inženýrská
-1-

.....
děkan

V Praze dne 23.10.2020

Prohlášení

Tímto prohlašuji, že jsem svoji diplomovou práci vypracovala samostatně a použila pouze uvedené podklady.

Nemám závažný důvod nesouhlasit s použitím této školní práce ve smyslu §60 Zákona č. 121/2000 Sb., o právech souvisejících s právem autorským a o změně některých zákonů (autorský zákon).

V Praze, 2021 .....

Bc. Diana Mária Krupová

Acknowledgement

I would like to express my gratitude to my supervisor, Jesús Guillermo Contreras Nuño, for his guidance, valuable advice and also for providing me with an opportunity to join the ALICE collaboration and to work on the MFT project. I could not have imagined having a better advisor for my master studies. I would also like to thank to Stefano Matthias Panebianco, who guided me throughout this work, answered all my questions and with whom it has always been a pleasure to work. I would also like to thank Luis Gustavo Perreira for many important skills learned while working with him. Last but not least, sincere thanks to the most beloved ones: especially Filip and all family members and friends who endlessly supported me.

Bc. Diana Mária Krupová

Název práce:

Studium vlastností detektoru Muon Forward Tracker pro upgrade experimentu ALICE

Autor: Bc. Diana Mária Krupová

Obor: Experimentální jaderná a částicová fyzika

Druh práce: Diplomová práce

Vedoucí práce: prof. Jesús Guillermo Contreras Nuño, PhD.

Abstrakt:

Muon Forward Tracker (MFT) představuje součást vylepšení systému detektorů ALICE během Long Shutdown 2 na LHC. MFT je nový detektor, který k detekci částic využívá křemíkové ALPIDE senzory. Tato práce je věnována studiu vlastností detektoru MFT a zahrnuje výsledky kvantitativní analýzy kvalifikačních procedur. Zároveň se zde zkoumá možnost využití detektoru MFT k měření fotoprodukce ρ mesonů v ultraperiferních srážkach, což dále přispívá k charakterizaci detektoru pro studium různých fyzikálních procesů.

Klíčová slova: CERN, ALICE, křemíkové detektory,
MFT, ALICE upgrade, fotoprodukce

Title:

Performance studies of the Muon Forward Tracker for ALICE upgrade

Author: Bc. Diana Mária Krupová

Field of study: Experimental Nuclear and Particle Physics

Thesis type: Master's thesis

Supervisor: prof. Jesús Guillermo Contreras Nuño, PhD.

Abstract:

The Muon Forward Tracker (MFT) is being added to the ALICE detector system as a part of undergoing major upgrades during Long Shutdown 2 at the LHC. The MFT is a new tracking detector using the ALPIDE silicon sensors as the active detection element. This work is dedicated to performance studies of the MFT. Results of quantitative analyses of the qualification procedures are reported. The performance is further studied by exploring MFT prospects for the measurement of ρ meson photoproduction in ultra-peripheral collisions in Run 3, aiming at a better understanding of the detector tracking performance.

Keywords: CERN, ALICE, silicon detectors,
MFT, ALICE upgrade, photoproduction

Physics isn't the most important thing. Love is.

RICHARD FEYNMAN

in a letter to Mrs. Chown, whose son, Marcus Chown, studied under Richard Feynman at the California Institute of Technology. Marcus was eager to get his mother to be more interested in science. After asking Feynman to write to her to spark her interest in physics, the letter was not what Marcus had expected [1].

Contents

Preface **1**

1 The ALICE detector and the Muon Forward Tracker **3**
1.1 CERN and the LHC . . . 3
1.2 A Large Ion Collider Experiment . . . 4
1.2.1 ALICE layout and subdetectors in Runs 1 and 2 . . . 4
1.3 ALICE upgrade for Run 3 . . . 7
1.3.1 Upgrade of the computing system . . . 8
1.3.2 The ITS upgrade . . . 10
1.4 The Muon Forward Tracker . . . 11
1.4.1 The MFT layout . . . 11
1.4.2 Ladder structure . . . 12
1.4.3 Disk and global support structure . . . 12

2 ALPIDE silicon sensors **15**
2.1 Silicon detectors in high-energy physics . . . 15
2.1.1 Silicon band structure . . . 15
2.1.2 The p-n diode junction . . . 16
2.1.3 CMOS technologies . . . 17
2.2 ALPIDE sensors . . . 18
2.2.1 ALPIDE front-end circuitry . . . 19
2.2.2 Monolithic Active Pixel Sensor . . . 20
2.3 Chip performance and tests . . . 21

3 Recent ALICE measurements and new physics prospects for Run 3 **23**
3.1 Physics motivation for ALICE upgrade and the addition of MFT 23
3.1.1 Current physics limitations . . . 24
3.2 Open heavy flavour . . . 24
3.2.1 Nuclear modification factor . . . 25
3.2.2 Heavy-flavour correlations and jet observables . . . 27
3.2.3 Quarkonia . . . 27
3.3 Low-mass dileptons . . . 29

3.4 UPC: recent measurements and prospects . . . 30
3.4.1 Ultra-peripheral Pb–Pb collisions . . . 30
3.4.2 UPC prospects with ALICE for Run 3 . . . 35

4 Commissioning of MFT ladders 37
4.1 Hybrid Integrated Circuit and Ladder Assembly . . . 37
4.2 Ladder quality assurance . . . 38
4.2.1 Smoke test . . . 39
4.2.2 Electrical tests . . . 39
4.2.3 Ladder functional tests . . . 39
4.3 Ladder qualification analysis . . . 47
4.3.1 Yield of conformal ladders . . . 47
4.3.2 Power consumption . . . 48
4.3.3 Threshold-noise characteristics . . . 48
4.4 Dead and noisy pixels . . . 49
4.5 Full MFT assembly and installation . . . 49

5 MFT tracking performance for ρ meson photoproduction 55
5.1 MFT tracking . . . 55
5.1.1 MFT standalone tracking . . . 56
5.1.2 MFT standalone tracking workflow . . . 56
5.1.3 MFT standalone track parameters . . . 59
5.1.4 Kalman filtering . . . 59
5.1.5 Vertex position estimation: reducing the combinatorics . 60
5.2 MFT perspective for ρ meson in Run 3 . . . 60
5.2.1 Standalone MFT tracks . . . 60
5.2.2 Track pairs . . . 61
5.2.3 CA track pairs . . . 66
5.2.4 Conclusions . . . 66

6 Summary and outlook 69

List of Figures

1.1 The layout of the ALICE detector in Run 2. 5
1.2 Layout of the ITS detector in Run 2. 6
1.3 A longitudinal cross section view of the ALICE Muon Spectrometer. 6
1.4 ALICE detector in Run 3 configuration after the upgrade. . . . 7
1.5 Positioning of the MFT detector in ALICE. 12
1.6 Layout of one half of the MFT detector. 13
1.7 Details of the MFT ladder in top exploded view and bottom view. 14
1.8 Ladder after the assembly, prepared for the qualification tests. . 14
1.9 Schematic figure of Half-Disk-0. 14

2.1 A diagram comparing the electron band structures of metals, semiconductors and insulators. 16
2.2 Cross section through the active devices of a CMOS based on a p-type substrate. 18
2.3 In-pixel hit discrimination block diagram and signal flow. 19
2.4 In-pixel front-end circuitry of the ALPIDE chip. Taken from [25]. 19
2.5 Schematic cross section of a MAPS pixel in the Tower Jazz imaging CMOS with the deep p-well feature. 20

3.1 Diagram of prompt and displaced J/ψ decaying into dimuons. . 24
3.2 R_{AA} of muons from heavy-flavour decays in $2.5 < y < 4$ as a function of p_T in different centrality classes in Pb–Pb collisions at $\sqrt{s_{NN}} = 2.76$ TeV. 26
3.3 R_{AA} of D^0, non-prompt J/ψ and non-prompt D^0 in ALICE in central Pb–Pb collisions for $L_{int} = 10$ nb^{-1}, taken from [27]. . . 26
3.4 Expected uncertainties on the measurement of R_{AA} of the ψ', in the scenario without and with MFT. 29
3.5 Event display of a candidate event for vector meson photoproduction at forward rapidity. 30
3.6 The cross section for coherent ρ^0 photoproduction in UPC for the three models compared with the ALICE result. 33

3.7 Excitation function for coherent and exclusive ρ^0 production with results from ALICE and STAR included. 33
3.8 Invariant mass distribution of pion pairs. 34
3.9 Cross section for the coherent photoproduction of ρ^0 vector mesons in Pb–Pb UPC as a function of rapidity with the predictions of the different models. 34
3.10 Invariant mass distribution of pion pairs with different components. 35
3.11 The dependence of the γA cross section for the coherent production of the ρ^0 meson and the corresponding power-law fit shown. 36

4.1 Chips positioning in the ALICIA machine. 38
4.2 Test bench used for the smoke test. 39
4.3 Test bench hardware for functional tests without back-bias voltage: $V_{\mathrm{BB}} = 0$ V. 40
4.4 Test bench hardware for functional tests with the back-bias voltage set to $V_{\mathrm{BB}} = -3$ V. 40
4.5 An overview of the steps performed by a threshold test. 42
4.6 A threshold S-curve for the front-end pixel chip. 42
4.7 Result of the threshold scan for chip 6 in ladder HIC_3182. . . . 44
4.8 The main measurement parameters associated with eye diagrams [45]. 45
4.9 Functional block diagram of the Data Transmission Unit and the related digital module DTU logic. 46
4.10 Measured eye diagram for chip 8 in ladder HIC_3182. 47
4.11 Results of electrical test: Power consumption of ladders is electrical tests A, B, and C. 50
4.12 Statistics on threshold and noise values: threshold mean without back-bias (a), threshold mean with back-bias (b), noise mean without back-bias (c), noise mean with back-bias (d). . . . 51
4.13 Number of dead pixels per chip in digital scan with $V_{\mathrm{BB}} = 0$ V (a) and with $V_{\mathrm{BB}} = -3$ V (b). Number of dead pixels per chip in threshold scan with $V_{\mathrm{BB}} = 0$ V (c) and with $V_{\mathrm{BB}} = -3$ V (d). 52
4.14 The MFT half-cone assembled inside the barrel. The picture also show cables, cooling tubes and a part of the Fast Interaction Trigger (T0C+). 53
4.15 Fully assembled MFT integrated with FIT inside the barrel with the beam pipe in the center. 53
4.16 MFT with beam pipe and the ITS Outer Barrel installed in the ALICE cavern. 54

5.1 Coordinate system used for MFT tracking. 57

5.2 The Cellular Automaton algorithm, where a track is a continuous chain of neighbouring cells with segments connecting clusters in consecutive disks. 57
5.3 LTF algorithm: an association of one cluster to a track seed, where R_{cut} represents the search radius. 58
5.4 Transverse momentum distributions of standalone tracks reconstructed with the MFT and of corresponding MC tracks. . 61
5.5 Number of clusters per MFT track for both CA and LTF tracks. 62
5.6 Pseudorapidity η distributions for CA and LTF tracks. 62
5.7 Transverse momentum p_T distributions for CA and LTF tracks. 62
5.8 Invariant mass and p_T distributions of ρ mesons reconstructed from track pairs. 63
5.9 Mass and transverse momentum p_T distributions for the ρ meson reconstructed from CA+LTF and LTF+LTF track pairs. 64
5.10 m, p_T, ϕ and y distributions for the ρ meson reconstructed from CA+LTF pairs. 65
5.11 Resolutions in m, p_T, ϕ, η for CA+LTF pairs. 66
5.12 Resolutions in m, p_T, ϕ, η for CA+CA pairs. 67

List of Tables

3.1 Cross sections and numbers of events in 13 nb^{-1} integrated luminosity for vector mesons in Pb–Pb collisions. 36

4.1 Summary of the amount of produced and bonded ladders and the yield of the conformal ones. 48

Preface

I'd take the awe of understanding over the awe of ignorance any day.

Douglas Adams: The Salmon of Doubt [2]

One of the primary goals of high-energy physics (HEP) is to discover and fully describe the elementary constituents of matter as well as the interactions between them, which are governed by four fundamental forces. The Large Hadron Collider (LHC) at CERN and all of its detectors were designed to provide new measurements towards this goal.

The LHC operation is currently interrupted: an upgrade of its components is underway with the objective to adapt them to the planned operation with a significantly higher luminosity. The ALICE detector, along with a novel MFT designed to improve the tracking capabilities of ALICE, are introduced in Chapter 1.

The MFT was designed to be used in conjunction with the current muon spectrometer. The 5 μm position resolution of the MFT will allow muon tracks originating from charm hadron decays to be distinguished from those originating from bottom hadrons. The presence of the MFT could help us, for example, to learn more about quarkonia and about their interactions with the deconfined medium created in heavy-ion collisions at the LHC.

The MFT is a silicon pixel detector. Chapter 2 contains the details of the use of silicon detectors in HEP and the technology incorporated in ALPIDE sensors used in the MFT. Each chip has a pixel density of half a million pixels in an active area of 4.5 cm^2, resulting in an improved resolution for high-precision track measurements. The MFT detector will be able to exploit the physics opportunities offered by the increased luminosity of future LHC runs.

Chapter 3 describes the physics motivation to build the MFT and an overview of ultra-peripheral collisions. The commissioning of the MFT with a summary of the results of the ladder qualification process is presented in Chapter 4.

In Chapter 5, the studies of the MFT performance are discussed: especially tracking and the prospects for the study of vector meson production in ultra-peripheral collisions are presented. The possibility to use MFT as standalone detector are explored here.

Finally, the conclusions and the long-term outlook can be found in Chapter 6.

Chapter 1

The ALICE detector and the Muon Forward Tracker

The ALICE detector, one of the four main detectors at the Large Hadron Collider (LHC) at CERN, is currently undergoing a major upgrade to prepare it for data taking during the LHC Runs 3 and 4, including an extensive upgrade of its individual subdetectors as well as the incorporation of completely new systems like the MFT. In this chapter, an overview of ALICE and its subdetectors is presented, along with the prospects arriving with the aforementioned upgrade with a focus on the MFT.

1.1 CERN and the LHC

After the establishment of CERN in 1954, a few breakthrough accelerators of that age were built and operated: the Proton Synchrotron (PS) and the Super Proton Synchrotron (SPS). One of the triumphant discoveries from the $p\bar{p}$ collisions programme at the SPS was the discovery of the $W^{\pm}$ and Z^0 bosons, the massive gauge bosons intermediating the weak interaction, by the UA1 and UA2 experiments.

Currently, we live in the era of the Large Hadron Collider, the LHC. It is the largest particle accelerator in the world. The placement of the LHC inside a 27-kilometer tunnel tens of meters underground makes use of the tunnel that was previously excavated for the Large Electron-Positron (LEP) collider at CERN. The first LHC run[1] started in 2009. After the upgrades that took place during the Long Shutdown 1 (LS1, 2013-2015), the second operational LHC run (Run 2) started in 2015 and lasted for three years. Currently, we are in the period of the Long Shutdown 2 (LS2), which was extended up until 2022.

[1]LHC operates in three-year periods called Run 1, Run 2 and so on, according to a schedule that is planned for up to twenty years ahead.

During the LHC Run 2, the protons were made to collide at a centre-of-mass energy $\sqrt{s} = 13$ TeV for pp collisions. One month each year of an LHC run is dedicated to heavy-ion physics, colliding lead ions (^{208}Pb) on either p–Pb (reaching $\sqrt{s_{\mathrm{pN}}} = 8.16$ TeV) or Pb–Pb collisions (at $\sqrt{s_{\mathrm{NN}}} = 5.02$ TeV) [3]. A similar schedule is planned for Run 3 and beyond [4].

1.2 A Large Ion Collider Experiment

ALICE, standing for *A Large Ion Collider Experiment*, is aimed at the study of head-on heavy-ion collisions, where the detector needs to be capable of measuring a large amount of particles originating in the collision to reconstruct their number, mass, type, or energy.

The search for the QGP originated in 1986 at the SPS and Brookhaven AGS (Alternating Gradient Synchrotron) simultaneously. Later, in 1987 and 1990, respectively, it was decided that the LHC would collide heavy ions as well as protons. At that time, RHIC (Relativistic Heavy Ion Collider) was approved. One of the challenges for the new general purpose heavy-ion detector was to achieve good resolution at both high and low momentum, with the large dynamic range required for the measurement of momenta ranging from tens of MeV to over 100 GeV [5].

1.2.1 ALICE layout and subdetectors in Runs 1 and 2

During the LHC Run 1 and 2, the experiment consisted of 17 different detection systems [5]; each of them with different technology choices and specific methods of detecting particles. A schematic view of ALICE in Run 2 is shown in Fig. 1.1. The ALICE detector and its performance are described in Ref. [7, 8]. The central barrel, containing the tracking detectors and covering the pseudorapidity $-0.9 < \eta < 0.9$ is located inside a solenoid magnet that creates a magnetic field of 0.5 T parallel to the beam line.

The innermost detector, placed as close as possible to the interaction point (IP), is the Inner Tracking System (ITS). The ITS aims at identifying and localising the primary vertices with μm accuracy and reconstructing the secondary vertices originating from the decays of unstable particles or resonances. For Run 2, the ITS is made of three parts (see Fig. 1.2) each with two layers, the parts are based on silicon pixel, drift and strip detectors, respectively. The silicon pixel detector (SPD) makes up the two innermost layers with about 10^7 pixels covering the pseudorapidity interval $|\eta| < 2$ and $|\eta| < 1.4$ for the inner and outer layers, respectively.

Besides the ITS, the Time Projection Chamber (TPC) is very important for tracking at central rapidities. The TPC provides three-dimensional (3D)

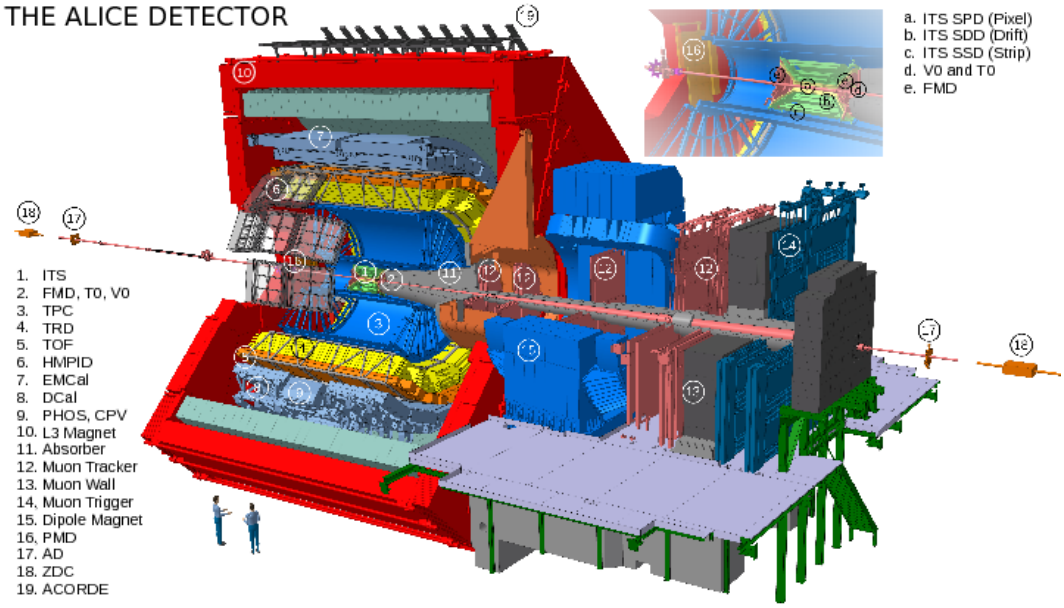

Fig. 1.1: The layout of the ALICE detector in run Run 2 with all the sub-detectors labelled with their acronyms. Taken from [6].

information for tracking and momentum measurement together with particle identification (PID) via the measurement of the specific energy loss. The TPC is an electronically read gaseous detector delivering direct 3D track information: for each point on the track, x, y and z coordinates are measured simultaneously. The TPC at ALICE consists of a double cylinder around the beam pipe, 5 m long, centred on the IP and inside the solenoid magnet [10]. A 100 kV central electrode separates the two drift volumes, providing an electric field for electron drift. The TPC acceptance covers the pseudorapidity region $|\eta| < 0.9$.

The occurrence of transition radiation (TR) is also extensively used for detecting particles; in ALICE, it is the main mechanism of detection in the ALICE Transition Radiation Detector (TRD) [11]. Highly relativistic particles (Lorentz factor $\gamma \gg 1$) emit photons when crossing from a medium with one dielectric constant into another. While the emission probability for such photons is small, its conversion leads to a large energy deposit compared to the average energy deposit via ionisation. The γ-dependent effect of TR is extremely valuable for PID at high energies: in a wide momentum range (1–100 GeV/c), electrons are the only particles producing TR, which can be used for the electron identification and separation of electrons from kaons or pions.

In ALICE, the main purpose of the Time-of-Flight (ToF) detector is the PID in a large part of the phase space. The ToF detector uses an array of

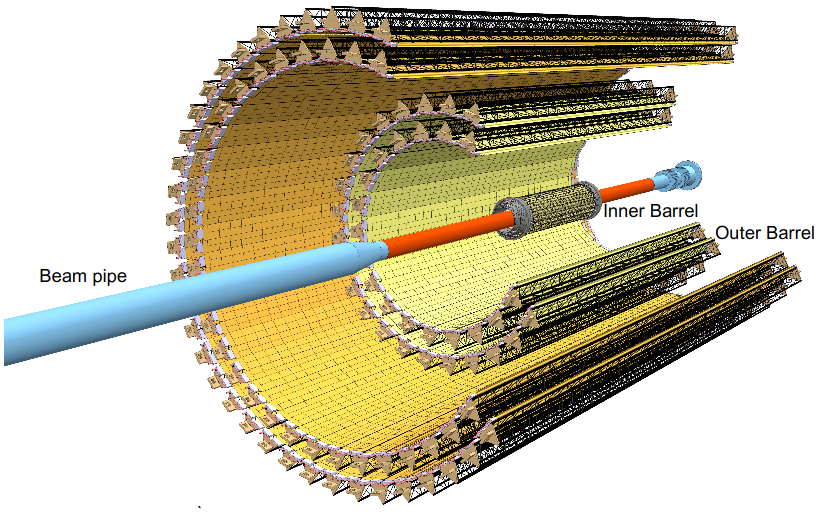

Fig. 1.2: Layout of the ITS detector in Run 2. Taken from [9].

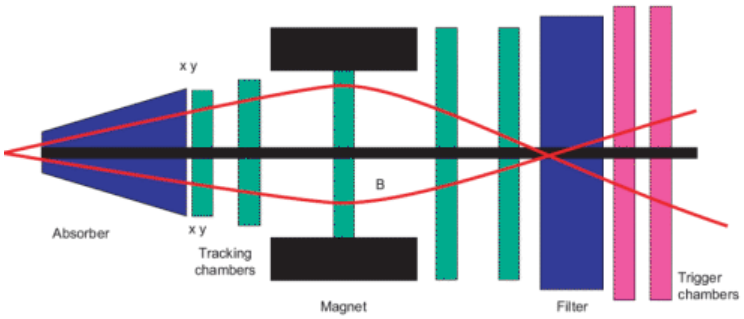

Fig. 1.3: A longitudinal cross section view of the ALICE Muon Spectrometer. Taken from [12].

multi-resistive plate chambers (MRPCs) covering a cylindrical surface around the IP. A ToF measurement is one of the methods to obtain the particle velocity. The velocity then serves for the PID: when the momentum is measured simultaneously, it is possible to reconstruct the charge and mass of the produced hadrons. The ToF detector measures the stopping time, while the collision time is measured with extreme precision (~ 25 ps at high multiplicities) by two sets of twelve Cherenkov counters, forming the T0 system, mounted tightly around the beam pipe. The ToF pseudorapidity coverage is $|\eta| < 0.8$.

The ALICE Muon Spectrometer [13] is designed to study open heavy flavour and quarkonia production via the dimuon decay channels. The schematic cross section of the spectrometer is shown in Fig. 1.3. The spectrometer consists of the front absorber, a high-granularity tracking system of 10 detection planes, a 3 Tm dipole magnet, a muon filter wall followed

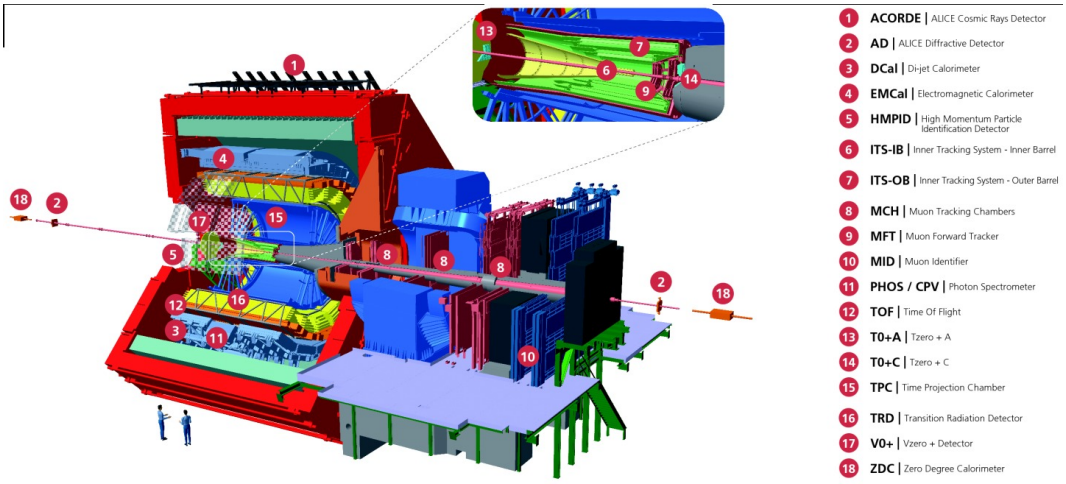

Fig. 1.4: ALICE detector in Run 3 configuration after the upgrade. Taken from [16].

by trigger chambers and the inner beam shield. The absorber, designed to absorb hadrons and photons from the interaction vertex, is made of carbon, steel, tungsten and concrete. It is located inside the solenoid magnet, weighs 50 tons and is 4.13 m long. For tracking, the muon spectrometer uses cathode pad chambers to achieve a space resolution of 100 μm. The pad chambers are organised in five stations composed of two planes to get two-dimensional position information. Four planes of 18 resistive plate chambers (RPCs) are used in the trigger chambers. The chambers are arranged in two stations and cover a total surface of 140 m^2.

The ALICE Zero Degree Calorimeter (ZDC) [14] consists of two sets of small, very compact calorimeters, each of which is located on one side of the IP, more than 100 m away along the beam pipe. The measurement of the energy carried away by the spectator nucleons from the heavy-ion collision in the forward direction is performed by the ZDC separately for neutrons and protons.

The V0 detector [15] consists of two arrays of scintillator counters used to select interactions and to reject beam-related background events. The two arrays, V0-A and V0-C, cover the pseudorapidity ranges $2.8 < \eta < 5.1$ and $-3.7 < \eta < -1.7$.

1.3 ALICE upgrade for Run 3

The ALICE upgrade during the Long Shutdown 2 (LS2) was designed to exploit to the fullest the scientific potential of the future LHC. The ALICE layout

together with all the detection systems after the upgrade can be seen in Fig. 1.4. The upgrade during LS2 includes [17]:

- a smaller diameter beam pipe;
- the ITS upgrade, see Sec. 1.3.2;
- the MFT, see Sec. 1.4;
- the TPC upgrade, consisting of replacement of the wire chambers with GEM detectors, and new pipelined read-out electronics;
- the read-out electronics upgrade of the TRD, the ToF detector and the Muon Spectrometer to achieve a higher operation rate;
- the upgrade of the forward trigger detectors;
- the upgrade of the online systems and the offline reconstruction and a new analysis framework, see Sec. 1.3.1.

After the LS2, the LHC will provide Pb–Pb collisions at an interaction rate of up to 50 kHz, corresponding to an instantaneous luminosity $\mathcal{L} = 6 \times 10^{27}$ cm^{-2}s^{-1} [17]. The upgrade strategy of ALICE took that into account, all of its upgrade plans were designed in a way to be able to process such a large rate; that means to improve tracking and vertexing capabilities, radiation hardness and, last but not least, to be able to accumulate enough statistics for the upgrade physics programme.

1.3.1 Upgrade of the computing system

During the LHC Run 3 and 4 ALICE needs to integrate a luminosity of 13 nb^{-1} for minimum bias Pb–Pb collisions together with dedicated p–Pb and pp reference runs.

To minimise the cost and requirements of the computing system for data processing and storage, the ALICE Computing Model for Runs 3 and 4 is designed for a maximal reduction of the data volume read out from the detector as early as possible during the data flow. The zero-suppressed data of all collisions will be shipped to the O^2 (Online-Offline computing system) [18] facility at the anticipated interaction rate of 50 kHz for Pb–Pb collisions or 200 kHz for pp and p–Pb collisions.

The raw data will first be rapidly reconstructed using online cluster finding and first fast tracking using an early calibration based on average running conditions. The data produced during this stage will be stored temporarily. Taking advantage of the duty factor of the accelerator and the experiment, the

second reconstruction stage will be performed asynchronously, using the final calibration to reach the required data quality.

The O^2 facility will be sufficient to perform both the synchronous fast reconstruction and asynchronous reconstruction during data taking.

O^2 architecture

In the O^2 architecture [18], designed to support both online synchronous data reduction and asynchronous and iterative data processing, the FLPs (First Level Processors) read out the raw data samples over the GBT-based front-end links and optical links, where the data are compressed by a factor of 2.5.

All the FLPs produce Sub-Time Frames (STFs), which are subsequently dispatched to the Event Processing Nodes (EPNs) for aggregation. The STFs related to the same time period from all FLPs are received by the same EPN and aggregated into a Time Frame (TF). The EPNs provide information about their capability to receive more data in the immediate future, and if an EPN breaks down or does not publish information about its availability, the EPN is removed from the list of possible destinations for the STFs to avoid possible data loss.

Calibration

A key to real-time data reduction is represented by the calibration. The calibration is integrated at different processing stages and allows us to minimise data transport and make results available as early as possible in the chain. The Condition and Calibration database (CCDB) is populated and used at all stages, synchronously and asynchronously. The synchronous phase is performed during the data taking. The asynchronous phase is decoupled from the data taking process. It provides analysable data in terms of individual collisions.

Data produced by the detectors are transferred to the common read-out units (CRU) in a continuous or triggered read-out mode over the GBT or DDL based read-out links. The triggered data is tagged with the LHC clock information. The continuous streams of data samples are split into heartbeat frames (HBF) using periodically occurring heartbeat triggers (HB) distributed synchronously.

The HBFs are accumulated into STFs during a period of the order of 22 ms. All FLPs produce STFs, which could be empty for those FLPs receiving data from triggered detectors inactive during the corresponding time period. The data are compressed and multiplexed in the CRUs and transferred to the memory of the FLPs.

The reduction of the raw data volume starts with the FLPs by converting raw to clusterised data and compressing by lossless algorithms. In the following

lossy data reduction on the EPNs, clusters with no chance to contribute to physics analyses[2] are rejected.

The O^2 facility, located at the experimental area at Point 2, will include all the FLPs, EPNs, networking and data storage. It will also provide interfaces with the Grid and the permanent data storage at the Tier 0.

Quality Control

Quality Control (QC) is intensively used in all processing stages. The feeding of the QC results in a dedicated database is ensured by data sampling at all levels. The aim of data QC is to provide a prompt feedback on the quality of the data being recorded, but also serves a an important tool for the subsequent asynchronous reconstruction or calibration.

The QC system uses user-defined algorithms to generate and populate the monitoring objects such as histograms. The quality assessment of these objects comes next, either at the same time or later in a separate step. The monitoring objects as well as the degree of their quality are stored and made available for visualisation or post-processing, where the capacity to trend the monitoring objects and results over time is one of the most important aspects.

Each detector provides a specific number of monitoring objects produced at each stage. The received data at different stages of the data flow are used by the QC system to provide objects: histograms, graphs, or values and a quality assessment of each object by the setting of different quality flags, e.g. good, bad or warning.

Although the QC results could be analysed manually, the risk for the latency introduced by human checks is too high. Therefore, automatic checks are used to categorise data in a framework with a set of common tools to check the quality of the monitoring data. For example, we can assess whether the mean value or standard deviation of a specific histogram is below a certain limit. The automatic checks are important for shifters to make evaluations of the data quality and to make decisions on the continuation of data taking.

1.3.2 The ITS upgrade

During LS2, the radius of the beam pipe will get reduced from 29.0 mm to 17.2 mm. For a tracking detector to reach an optimal performance, it should be placed as close to the IP as possible, as many particles of interest live for a very short time before decaying into daughter particles.

A grouping of the seven layers in two separate barrels is provided for the new ITS, see Fig. 1.5. The three innermost layers form the Inner Barrel,

[2]The data which are rejected correspond to noise, δ-rays background or beam-gas collisions.

while the four outermost layers compose the Outer Barrel. The ITS layers are azimuthally segmented in units named staves. The staves serve as an equivalent of the ladder structures used in the MFT and are mechanically independent.

The spatial resolution of the upgraded ITS [9] will get improved by a factor of 3 as a result of placing the first layer of the new ITS detector closer to the beam pipe; the reduction of the material budget per layer; and thanks to the new geometry and segmentation with a reduced pixel size from 50×425 μm^2 to 30×30 μm^2 with a thickness of 50 μm.

A novel CMOS Monolithic Active Pixel Sensor (MAPS) ALPIDE, see also Chapter 2, used for the MFT detector as well, has been developed to reduce the material budget and to improve the granularity. The ALPIDE sensors have both read-out and sensor implemented on a single silicon substrate.

1.4 The Muon Forward Tracker

The design of the MFT, a new tracking detector for ALICE at forward rapidities, was constrained by the requirements expressed by ALICE and the LHC [17]. The importance and layout of the detector were stated in the Addendum to the ALICE upgrade Letter of Intent [19], the design itself was presented in the MFT Technical Design Report [20]. In conjunction with the upgrade of the ITS, the upgrade programme aims to reach a high precision measurement of hard processes, serving as sensitive probes of the deconfined medium.

1.4.1 The MFT layout

The MFT has a conical shape surrounding the beam pipe and is placed between the IP and the hadron absorber. A general view of the MFT is shown in Figs. 1.5 and 1.6. The detector consists of two half-cones. Each MFT half-cone consists of 5 half-disks positioned along the beam axis in the direction of the Muon Spectrometer at $z = -460$, -493, -531, -687, -768 mm from the IP. The MFT covers the pseudorapidity acceptance $-3.6 < \eta < -2.45$.

A half-disk consists mainly of sensor ladders, containing 2 to 5 silicon pixel sensors soldered to a flexible printed circuit (FPC). The materials used have been selected with consideration to keep the material budget[3] minimised: it amounts to less then 0.6% of a radiation length X_0 per disk.

[3]The radiation length X_0 is commonly used to determine the amount of material traversed by particles in a detector. The detector thickness expressed in units of X_0 is called the material budget.

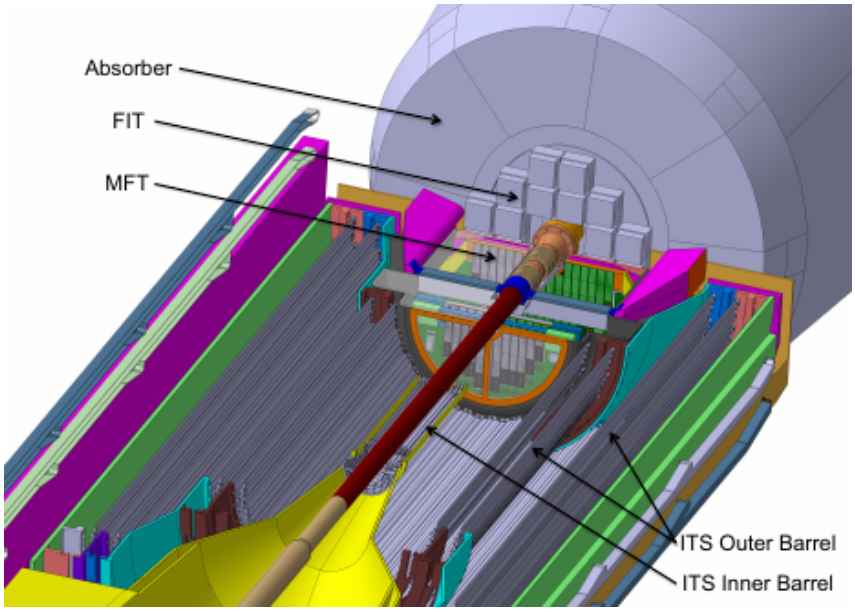

Fig. 1.5: Positioning of the MFT detector in ALICE. The layout of the upgraded ITS is also shown. Taken from [20].

Pixel sensor

The basic detection element of the MFT is a silicon pixel sensor ALPIDE that is further described in Chapter 2.

1.4.2 Ladder structure

The silicon pixel sensors are integrated with mechanical ladder structures that hold the sensors and ensure electrical links between the sensors and the readout electronics. The ladder consists of the following elements (Fig. 1.7): the stiffener, serving as a mechanical support, the silicon pixel sensors, and the FPC. An actual photo of the ladder in a protective cover is shown in Fig. 1.8.

The Hybrid Integrated Circuit (HIC) consists of the sensors laser soldered to the FPC with a gap of 100 μm between sensors. The ladder assembly and qualification procedure are further described in Chapters 2 and 4.

1.4.3 Disk and global support structure

The MFT consists of five disks, see Fig. 1.9. Each disk is subdivided in two half-disks, top and bottom, corresponding to the upper and lower half of the MFT. The first two of the disks (called disk 0 and 1) located closer to the IP are identical, while the remaining three disks are different and larger (disk 2, 3, and 4). Each disk is subdivided into two half-disks (see Fig. 1.9). Each

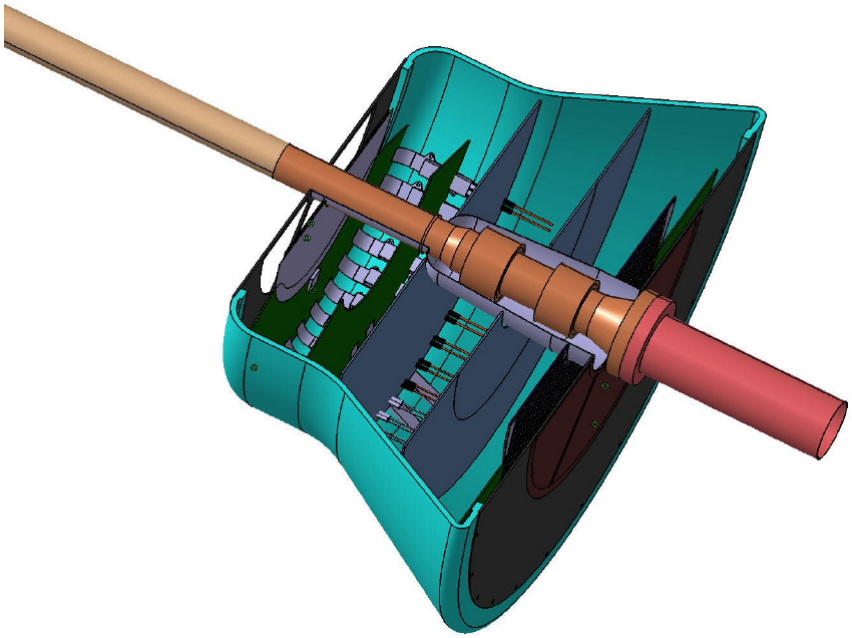

Fig. 1.6: Layout of one half of the MFT detector. Taken from [19].

half-disk has two detection planes, one on the front and one on the back side. The hermeticity of each half-disk is ensured by the overlap between sensors of the back and front planes.

A half-disk consists of a disk spacer, a disk support, two printed circuit boards (PCBs), and sensor ladders glued along their length on the half-disk spacer. The PCBs are equipped with connectors, DC-DC converters providing 1.8 V for the sensors and other electronic components.

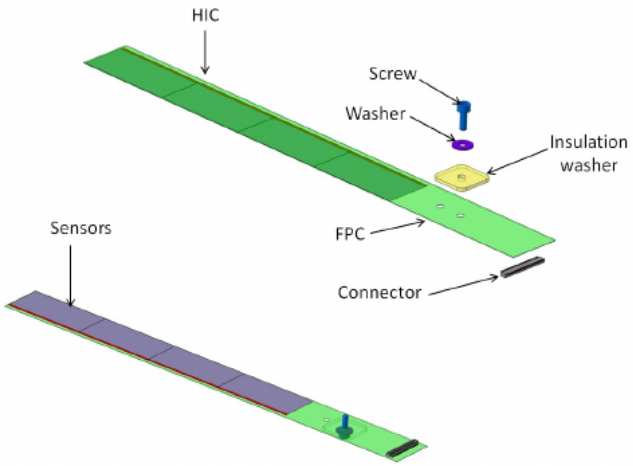

Fig. 1.7: Details of the MFT ladder in top exploded view and bottom view. Taken from [20].

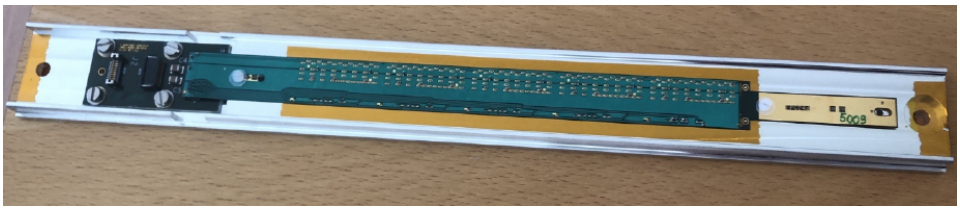

Fig. 1.8: Ladder after the assembly, prepared for the qualification tests.

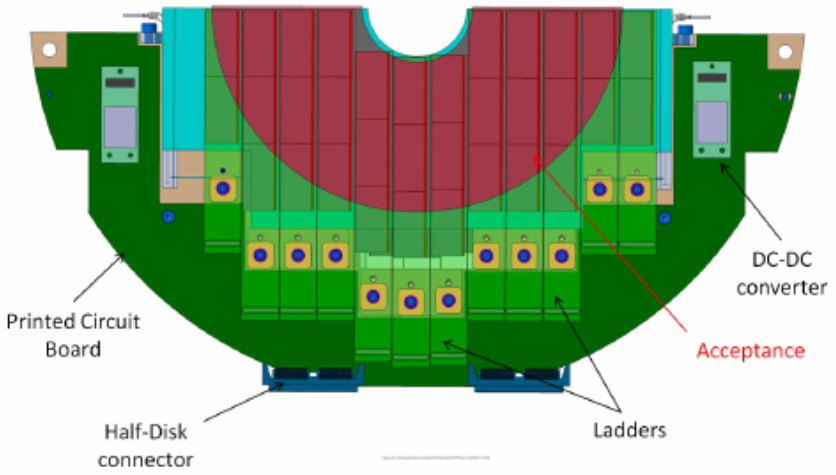

Fig. 1.9: Schematic figure of Half-Disk-0. Taken from [20].

Chapter 2

ALPIDE silicon sensors

ALPIDE (ALICE pixel detector) [9] is a pixel chip based on the TowerJazz 180 nm CMOS Imaging Process, developed by the ALICE pixel group for both the ITS and MFT upgrade. This chapter summarises the main ALPIDE characteristics along with the motivation to use silicon detectors to measure various attributes of particles created in HEP experiments.

2.1 Silicon detectors in high-energy physics

Historically, silicon detectors have enabled economically reasonable fiber-based optical communication, optical storage or high-frequency amplification. The revolution due to the technological developments used in everyday life, such as photography, display technology or lighting, would not arise without them. Their properties, low price and potential for numerous applications make them widely used in HEP.

The main detection element of the MFT, the focus of this work, is a semiconductor (silicon) ALPIDE sensor. In the following sections, we briefly illustrate how semiconductor detectors work and the different possibilities to operate them in HEP. A more detailed motivation can be found in the author's previous work [21].

2.1.1 Silicon band structure

The semiconductor properties of silicon originate from its band structure, as illustrated in Fig. 2.1. Electrons involved in the bonds between atoms occupy states in the valence band and they are localised in the proximity of the atoms. Electrons in the conduction band are not attached to any atom and they can easily move through the crystal under an electric field. The two bands are separated by an energy gap of 1.12 eV with no accessible states present.

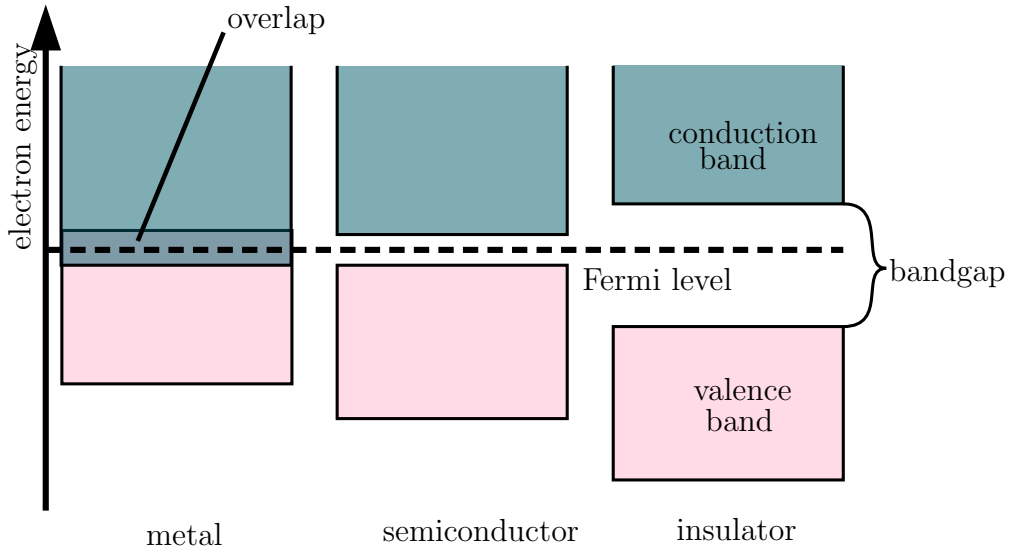

Fig. 2.1: A diagram comparing the electron band structures of metals, semiconductors and insulators.

At low temperatures near absolute zero, all the states in the valence band are occupied and all states in the conduction band are empty. Therefore, no free carriers are available for conduction and the material behaves as an insulator. With the temperature rising, electrons acquire thermal energy until they make a transition into the conduction band. The electron leaves behind an empty location in the valence band, known as a hole. Electrons and holes can also recombine.

Doping

The introduction of impurities into semiconductors is called *doping*. In the process of doping, atoms with either three or five electrons in the outer shell are introduced into the silicon crystal lattice. This process results in either silicon doped with acceptor atoms: the p-type, or with donor atoms: the n-type silicon.

2.1.2 The p-n diode junction

The p-n diode junction is a very basic, albeit one of the most important electronic structures. It can be used as a particle detector: a traversing particle, e.g. produced in a collision, generates electron-hole pairs in the depletion zone, which creates a charge signal.

The p-n junction is obtained by joining a p-type with a n-type extrinsic semiconductor together. While the p-type and n-type regions in the junction are separated in thermal equilibrium, the charge carriers, that is, the electrons

and holes, are homogeneously distributed in their volumes. Bringing the two parts into contact sets off a diffusion process of electrons into the p-type region and holes into the n-type region. A surplus of negative charge in the p-type region (positive charge in the n-type region) is created which generates an electric field counteracting the diffusion. Therefore, a region of non-mobile space charge is formed. A potential barrier V_{bi} is generated between the two space charge densities, preventing electrons and holes from diffusing further. No mobile charge carrier is present in the depletion zone, the central zone of the junction: a region on either side of the junction. It plays an important role in the physics of the MOS transistor.

An external voltage can be applied to a p-n junction in two ways: in forward bias and reverse bias, also called back bias. In a forward bias scenario, i.e., the positive terminal of the source is connected to the p-type side and the negative terminal of the source is connected to the n-type side, the voltage across the junction decreases from the equilibrium value V_{bi} by the externally applied positive voltage V to $V_{\mathrm{bi}} - V$ which shrinks the width of the depletion region.

If the diode is back biased, i.e., the positive terminal of the source is connected to the n-type side and the negative terminal of the source is connected to the p-type side, the depletion region becomes wider with increasing back bias voltage until a certain value of voltage, when the depletion region gets destroyed and a reverse current starts to flow through the diode.

The ALPIDE sensors can be be operated with back-bias voltage V_{bb}. To perform the qualification tests (see Chapter 4), two configurations were used: $V_{\mathrm{bb}} = 0$ V and $V_{\mathrm{bb}} = -3$ V.

2.1.3 CMOS technologies

ALPIDE sensors use the CMOS Monolithic Active Pixel Sensor (MAPS) technology for all layers. Complementary metal-oxide-semiconductor (CMOS) [22] is a type of MOSFET (metal-oxide-semiconductor field effect transistor) fabrication process allowing the fabrication of integrated circuits containing complementary and symmetrical pairs of p-type and n-type MOSFETs, thus creating elements for logic functions, widely used in microelectronics.

CMOS technology in its simplest form uses only n- and p-channel enhancement transistors as active devices, see Fig. 2.2. The regions between the individual electronic elements are covered by an oxide layer to reduce the parasitic capacitance. The source (S) and the drain (D) are heavily n-doped, and the thin gate oxide is covered by a polysilicon gate, which is aligned with the source and the drain. The p-channel transistor is placed in an n-doped well which controls the transistor threshold voltage. The devices are typically built into a wafer: a common p-type substrate, because p-doped wafers are easier and cheaper to produce. The devices are fabricated on a wafer by layering

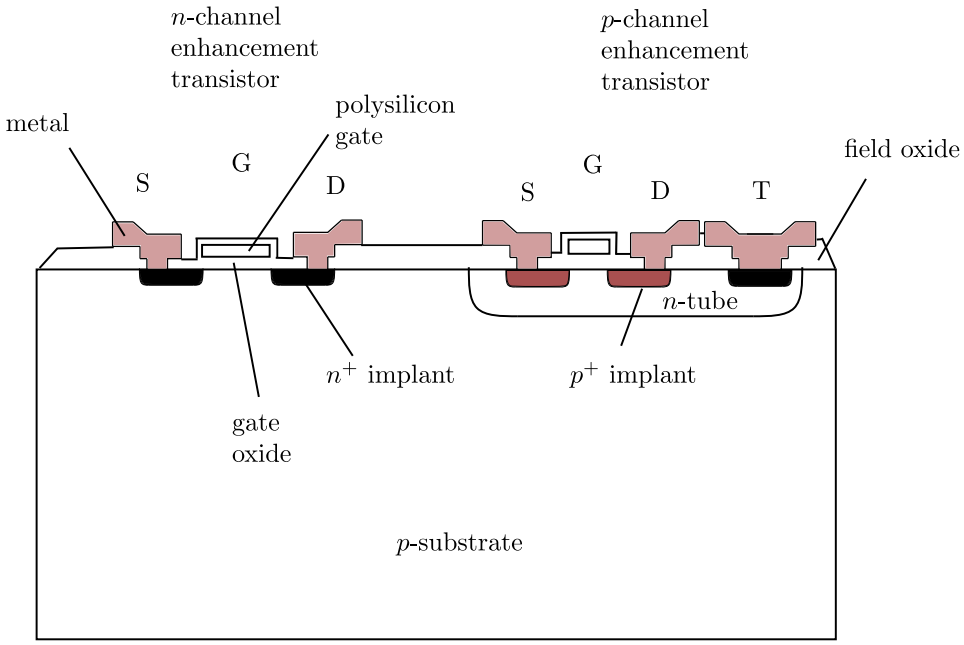

Fig. 2.2: CMOS technology. Cross section through the active devices of a CMOS based on a p-type substrate.

different materials in specific locations and shapes on top of each other via photolithographic and chemical processes.

The ability to fabricate both nMOS and pMOS on the same substrate made the CMOS technology so successful, e.g., as a radiation sensor, where the sensor and its front-end electronics are both embedded on the same wafer. Monolithic Active Pixel Sensors (MAPS) integrate the sensor matrix and readout in one piece of silicon. In this case, an n-well on a p-type epitaxial layer collects the signal charge generated by the ionising particle. The nMOS transistors are placed in a p-well shielding the source and drain junctions from the epitaxial layer, which is essential to collect all the signal charge. This solution has also been adopted for the ALPIDE sensors.

2.2 ALPIDE sensors

ALPIDE sensors are implemented on silicon wafers with a high resistivity epitaxial layer. A single chip measures 15 mm × 30 mm and contains half a million pixels distributed in 512 rows and 1024 columns.

The block diagram of the ALPIDE pixel cell is shown in Fig. 2.3. A `STROBE` signal controls a threshold level, applied to all pixels. The ALPIDE architecture also allows to apply reverse substrate bias V_{BB} to increase the total bias of

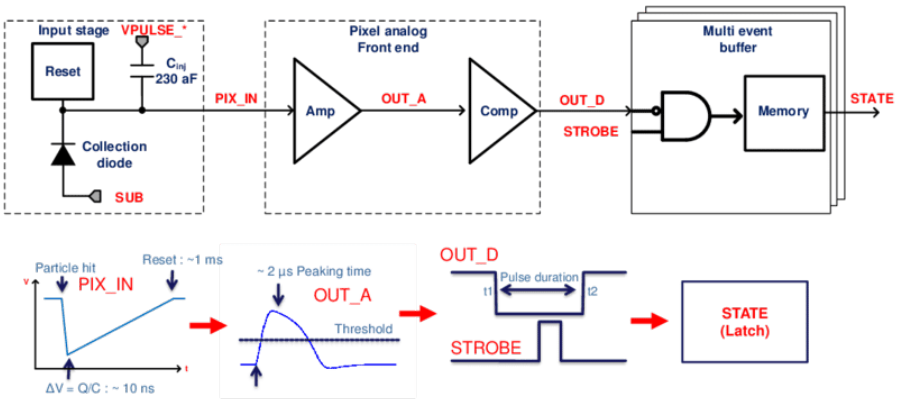

Fig. 2.3: In-pixel hit discrimination block diagram and signal flow. Taken from [23].

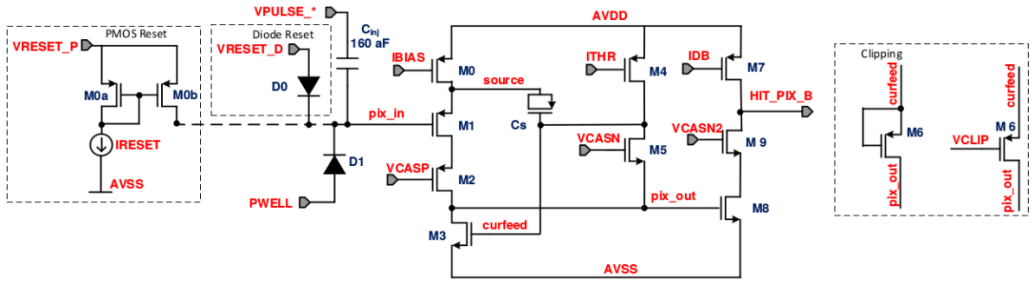

Fig. 2.4: In-pixel front-end circuitry of the ALPIDE chip. Taken from [25].

the collection diode. All analog signals required by the front-end are generated by a set of on-chip 8-bit digital-to-analog converters (DAC).

2.2.1 ALPIDE front-end circuitry

The process of charge amplification and discrimination can be understood from the internal front-end circuit [24] of the ALPIDE cell shown in Fig. 2.4.

A voltage drop in the `pix_in` node is caused either by the charge collected in the collection diode `D1` or injected through the capacitance C_{inj}. This allows for an additional current flow through the pMOS cascade (`M1, M2`) from the current source `IBIAS`, charging the `pix_out` node. The node is restored as the voltage becomes close to the gate potential `VCASN` of the `M5` transistor and its conductance is reduced. The value of the `VCASN` voltage thus sets the baseline of the `pix_out` potential. The current `ITHR` will therefore flow through the `curfeed` node, opening the `M3` transistor and discharging the `pix_out` node. The duration of the restoration process and the pulse shape can be adjusted

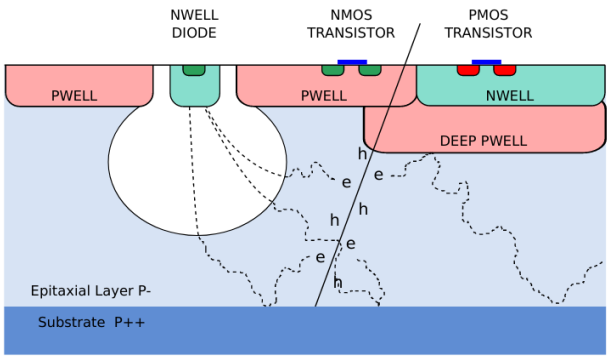

Fig. 2.5: Schematic cross section of a MAPS pixel in the Tower Jazz imaging CMOS with the deep p-well feature. Taken from [9].

with the `ITHR` current. The transistor `M7` becomes conductive again and the `curfeed` node is also restored.

2.2.2 Monolithic Active Pixel Sensor

In the MAPS implementation [26], the epitaxial layer is used as a radiation sensitive volume of the detector, with a diode n-well or p-epitaxy layer working as a charge collecting element. With the detector only partially depleted, the charge is collected mainly through a thermal diffusion mechanism. The volume spread of diffusing electrons created by the absorption of radiation is limited by a potential minimum in the middle of the epitaxial layer[1].

A potential barrier that deflects the generated electrons is formed between the lightly doped p-type epitaxial layer and the heavily doped p-type substrate. The signal charge is prevented from diffusing into the substrate by another potential barrier between the substrate and epitaxial layer.

The electrons, randomly diffused in the epitaxial layer due to the potential barrier between the lightly doped epitaxial layer and the heavily doped p-wells of the nMOS transistors, are guided towards the n-well of the collection diode.

A typical collection time is of the order of 100 ns. The detector active volume is limited to the epitaxial layer only (with a typical thickness of the order of 10 μm). The total amount of available charge created by the minimum ionising particle is a few hundreds of electrons.

Charged particles generate a thin trail of electron-hole pairs in the silicon (see Fig. 2.5). The entire amount of electrons created due to the passage of ionising particles will be collected, as there is only one p-n junction present in

[1]The minimum in the middle of the epitaxial layer is created thanks to a particular doping profile.

the pixel. The sensor is therefore able to detect particles regardless of where they hit the sensor.

2.3 Chip performance and tests

To ensure the quality of all sensors prior to mounting on the stave or the ladder, each chip is tested according to a defined test procedure, where high demands need to be met. For example, only one out of 10^5 pixels is allowed to be faulty. All the tests are performed with and without back-bias. A basic electrical test, also called *smoke test*, is performed first. The electrical and functional tests address the full electrical functionality of the chip and validate the signal generation in the epitaxial layer. The sensor response is studied using either light or a radioactive source.

During chip testing, a probe card is used to provide the electrical connection to the chip pads. Functional tests, where valid signal generation and full electrical functionality are addressed, include the read-out test, FIFO (first in–first out) scan, digital scan, threshold scan, noise occupancy scan, and eye measurement.

Later on, a very similar qualification process needs to be performed for the chips assembled in a ladder. The ladder qualification tests, the main focus of the author's work at CERN, are further described in Chapter 4.

Chapter 3

Recent ALICE measurements and new physics prospects for Run 3

Recent results in heavy flavour and quarkonia studies as well as in ultra-peripheral collisions (UPC) are reviewed in this chapter, along with the prospects of the upgraded LHC and ALICE. The focus is put on the new physics opportunities brought with the installation of the MFT. The future physics opportunities for high-density QCD at the LHC are described in [27]. The physics motivation for the MFT was presented in [20] and further expanded in [19]. The ALICE performance in Run 3 that complements the physics performance studies included in the Technical Design Reports of the detectors can be found in [28, 17]. Amongst the many other physics objectives of the upgraded ALICE detector [17], we will focus in this chapter on the motivation for the study of heavy flavours and charmonia. Finally, opportunities to study the behaviour of QCD at high energies and large partonic densities via UPC are discussed.

3.1 Physics motivation for ALICE upgrade and the addition of MFT

The presence of the MFT will enhance ALICE capabilities for detecting muons at forward rapidity. Mainly, it will generally improve all measurements performed by the Muon Spectrometer. On top of that, new physics will become accessible down to very low p_T: separation of prompt and displaced J/ψ or separation of charm and beauty decays. ALICE with the MFT will provide an excellent tool to perform such measurements.

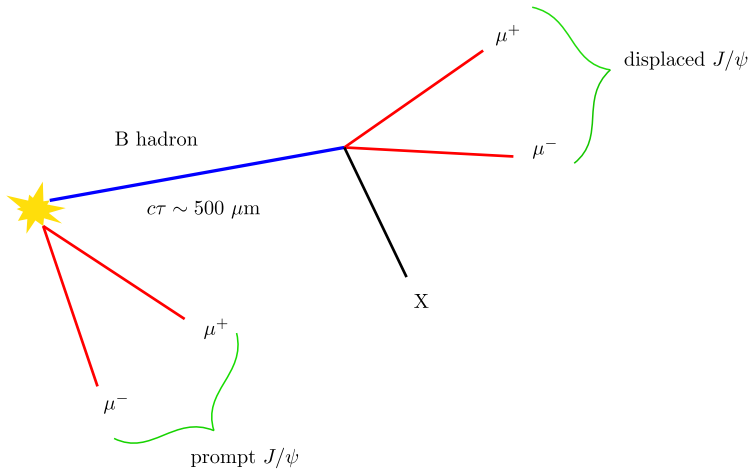

Fig. 3.1: Diagram of prompt and displaced J/ψ decaying into dimuons.

3.1.1 Current physics limitations

With the Muon Spectrometer alone, the measurements suffer from several limitations, primarily due to the multiple scattering induced on the muon track by the hadron absorber. Tracks from the Muon Spectrometer do not determine the region of the primary vertex. Information about the details of the vertex region is lost, which makes it impossible to distinguish the background represented by muons coming from semi-muonic decays of π and K mesons, often used in muon analyses. Limited details in the vertex region also prevent us from disentangling open charm from open beauty production or distinguishing between prompt and displaced J/ψ production, see Fig. 3.1.

3.2 Open heavy flavour

Charm and beauty quarks produced in hard scattering processes in the early stage of heavy-ion collision traverse the QGP medium and interact with its constituents through inelastic and elastic processes. These interactions, gluon radiation and collisional processes, may lead to the thermalisation of low-momentum heavy quarks. The large masses of charm and beauty quarks ($m_{\mathrm{c}} = 1.27$ GeV, $m_{\mathrm{b}} = 4.18$ GeV [29]) allow the heavy-flavour hadrons to serve as a unique probe of the early stages of the collision and, thanks to their long lifetime ($c\tau \sim 150$ μm and $c\tau \sim 500$ μm) provide information on all stages of the deconfined medium evolution.

The Run 3 of the LHC may open a new high-precision era for heavy-flavour measurements in HI collisions that will address several unresolved questions. With the upgrades of the machine and of the tracking detectors, the higher

accumulated statistics and higher precision will make it possible to quantify the properties of the QGP with heavy-flavour probes.

In ALICE, the track pointing resolution will be improved by a factor of 3 in the direction transverse to the beam line and by a factor of 5 in the longitudinal direction, down to values of 20 μm for tracks with $p_T = 1$ GeV/c. The MFT will allow for the separation of the primary vertices from secondary vertices with muons from D, B, and J/ψ decays. The key measurements expected to have a large impact on the characterisation of the QGP are discussed in the next sections.

3.2.1 Nuclear modification factor

The nuclear modification factor

$$R_{\mathrm{AA}}\left(p_{\mathrm{T}}\right) = \frac{1}{\langle N_{\mathrm{coll}} \rangle} \cdot \frac{\mathrm{d}N_{\mathrm{AA}}/\mathrm{d}p_{\mathrm{T}}}{\mathrm{d}N_{\mathrm{pp}}/\mathrm{d}p_{\mathrm{T}}}, \tag{3.1}$$

is used to study the evolution of the medium considering the energy loss of heavy quarks. Here, $\langle N_{\mathrm{coll}} \rangle$ is the mean number of binary collisions[1], $\mathrm{d}N_{\mathrm{AA}}/\mathrm{d}p_{\mathrm{T}}, \mathrm{d}N_{\mathrm{pp}}/\mathrm{d}p_{\mathrm{T}}$ are the production yields as a function of transverse momentum in nucleus-nucleus (AA) and pp collisions.

According to QCD, quarks should lose less energy than gluons when passing through the medium. This is due to the fact that in-medium gluon radiation is expected to increase with the colour-charge of the emitting particle. The energy loss should further decrease with increasing mass, due to the so-called dead-cone effect, where gluon radiation is suppressed below a certain radiation angle. Having a larger minimal angle below which no radiation occurs, heavy quarks radiate less gluons, which results in the observation of a smaller energy loss. Due to their colour charge, gluons, dominating the production of light hadrons, are expected to lose more energy than quarks, but also charm quarks are expected to lose more energy than beauty quarks due to their smaller mass. For the nuclear modification factors, all of the mentioned should result in

$$R^{\pi}_{\mathrm{AA}} < R^{D}_{\mathrm{AA}} < R^{B}_{\mathrm{AA}}. \tag{3.2}$$

The present status of heavy-flavour measurements in heavy-ion collisions at forward rapidity is shown in Fig. 3.2. The present measurement in the forward-rapidity region suffers from being inclusive and from being limited to high p_T.

Figure 3.3 shows the ALICE simulation results for D^0, non-prompt J/ψ, non-prompt $D^0, B^+ (\rightarrow \mathrm{D}^0\pi^+)$. With the high luminosity and the upgraded ITS in ALICE, the R_{AA} of light hadrons, charm hadrons and beauty hadrons can be clearly separated in a wide kinematic range.

[1] N_{coll} can be analytically derived from the Glauber model [30].

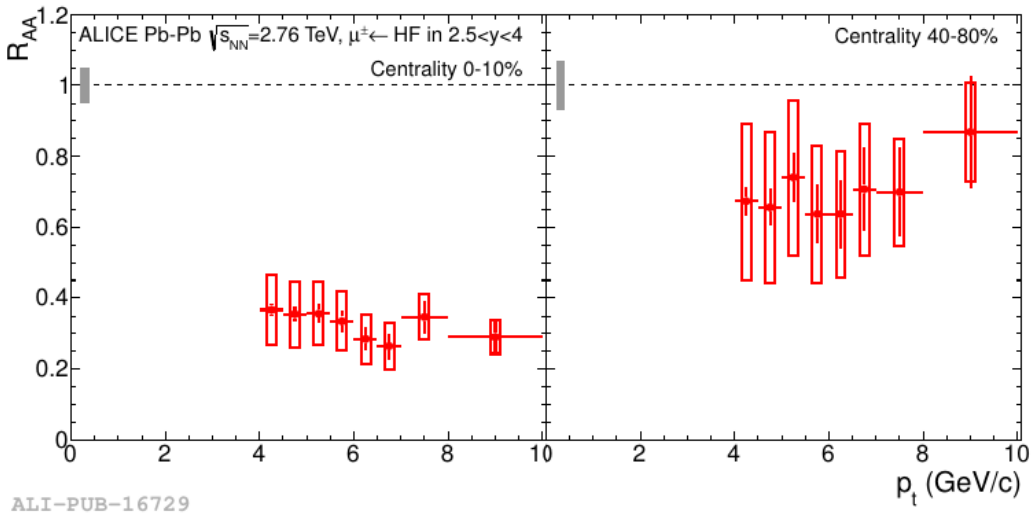

Fig. 3.2: R_{AA} of muons from heavy-flavour decays in $2.5 < y < 4$ as a function of p_T in different centrality classes in Pb–Pb collisions at $\sqrt{s_{NN}} = 2.76$ TeV. Open boxes represent the systematic uncertainty. Taken from [19].

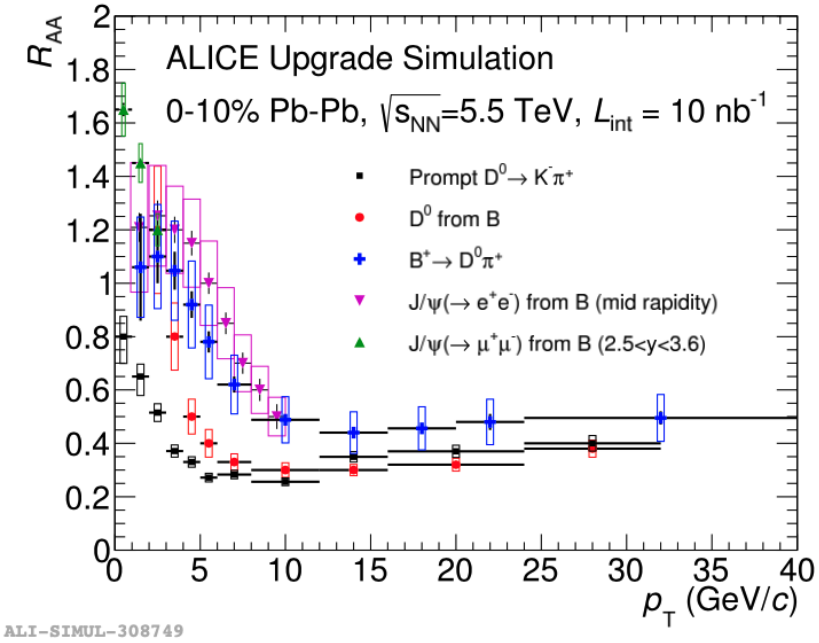

Fig. 3.3: R_{AA} of D^0, non-prompt J/ψ and non-prompt D^0 in ALICE in central Pb–Pb collisions for $L_{int} = 10$ nb^{-1}, taken from [27].

The MFT will allow us to measure the production cross section of muons from charm and beauty decays separately down to low p_T. The effect of a separate measurement provides a reference for the study of charmonium or bottomonium suppression in the QGP and measuring the charm and beauty R_{AA} separately allows us to test theoretical predictions for the energy loss of charm and beauty quarks in the medium.

3.2.2 Heavy-flavour correlations and jet observables

Heavy-flavour correlations

At LHC energies, even though the majority of heavy quarks are produced in primary hard scattering, an important fraction of c and b quarks originate from gluon splitting.

As heavy-ion calculations use pp generators as a baseline, they can be biased because of the different energy loss of quarks and gluons. A promising way to study these mechanisms in different kinematic ranges of c quarks comes from studying correlations between D and $\bar{D}$ mesons.

The study of open heavy-flavour correlations at forward and backward rapidity in p–Pb collisions provides information to test modifications of PDFs (parton distribution functions) in nuclei.

Heavy-flavour jet measurements

A new way to study possible modifications of charm fragmentation arise from a precise estimation of the suppression of D^0-tagged jets down to low p_T by measuring the R_{AA} of D^0-meson tagged jets in Pb–Pb collisions in ALICE at $\sqrt{s_{\mathrm{NN}}} = 5.02$ TeV. Similar measurements of c fragmentation in pp collisions will help to reduce uncertainties in theoretical calculations that describe heavy quark production at the LHC.

Heavy flavour measurements in small colliding systems

Further studies of the yields of the various c and b hadrons as a function of charged-particle multiplicity, as done in the past for strangeness production, may bring interesting information on the onset of medium effects.

3.2.3 Quarkonia

The larger experimental data samples in Run 3, combined with improved detector performance and measurement techniques, will allow us to significantly improve the current quarkonia measurements, with extended kinematic p_T coverage and allowing one to reach currently unobserved quarkonium

states, like $\Upsilon(3S)$. In ALICE, quarkonia are measured in the dimuon channel ($2.5 < y < 4.0$) and in the dielectron channel ($|y| < 0.9$). The addition of the MFT will allow ALICE to separate the prompt charmonium from the contribution from B meson decays at large rapidities.

Charmonia

Considering charmonia production, measurements are currently limited by a large combinatorial background and the impossibility to disentangle prompt and displaced production.

Charmonia production is the classical tool to investigate:

- suppression mechanisms due to dissociation of charmonia states in the medium (colour screening) [31],
- recombination mechanisms due to the relative abundance of available $c\bar{c}$ pairs in the deconfined medium [32],
- the interplay between suppression and recombination mechanisms.

Disentangling the contributions of prompt and non-prompt J/ψ and considering energy loss is necessary to understand the details of the J/ψ elliptic flow coefficient v_2 pattern, which will be facilitated with the higher luminosities of Run 3 and will be reachable with the ALICE central barrel. The projected ALICE measurements of inclusive J/ψ v_2 as a function of p_T for the centrality class 20-40% for $2.5 < y < 4.0$ can be found in [27]. Also, the measurement of higher harmonics such as v_3 will become available and provide further insight into charmonium production mechanisms.

The presence of the MFT detector will significantly reduce the uncertainties on the extraction of the ψ' signal by improving the signal over background (S/B) ratio and allow for a reliable separation of prompt and displaced J/ψ production. Currently, with the Muon Spectrometer alone, the S/B ratio ranges from 0.2% to 0.5% according to the p_T range [33]. Thanks to the capability of the MFT to access the details in the vertex region, both muon pairs, where at least one muon is produced within the hadron absorber, and muon pairs whose muons do not share a common origin, could be identified and rejected. The expected improvement with the MFT is shown in Fig. 3.4.

Quarkonia in p–Pb collisions

In the interpretation of Pb–Pb results, the measurements of quarkonium production in p–Pb collisions should be accounted for. Measurements of nuclear effects not resulting for the QGP creation in high-energy p–Pb collisions can alter the quarkonium yields.

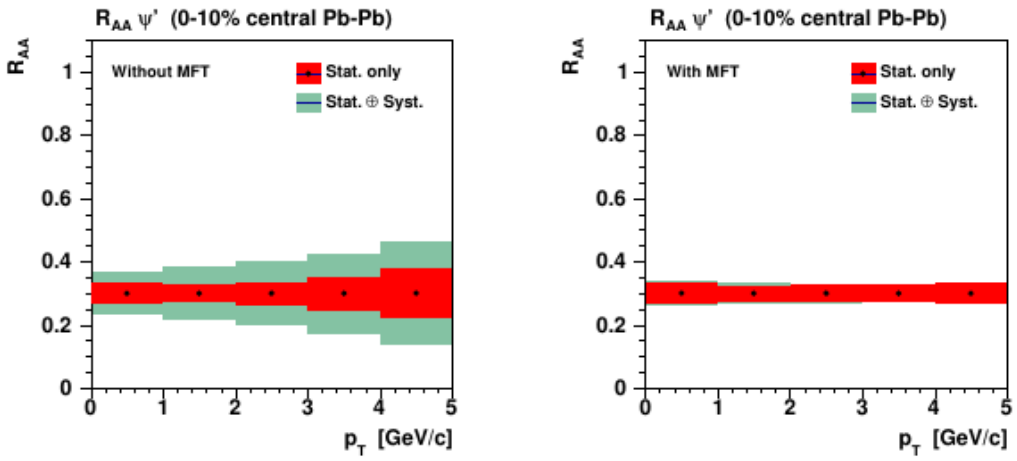

Fig. 3.4: Expected uncertainties on the measurement of R_{AA} of the ψ', in the scenario without and with MFT, where $R_{AA}(\psi') = 0.3$ is considered. Taken from [33].

Furthermore, the study of p–Pb collisions alone can bring interesting results: they could be used to probe the modification of the gluon densities in the nuclei or the interaction between pure heavy-quark bound states and light hadrons.

More importantly, forward-quarkonium production in p–Pb collisions is expected to be sensitive to low-x phenomena, such as gluon shadowing or saturation in the Pb nucleus, and to the coherent energy loss. The backward production on the other hand should be sensitive to the gluon antishadowing and to fully coherent energy loss.

3.3 Low-mass dileptons

Low mass vector meson (ρ, ω, φ) production provides key information on the hot and dense state of the the strongly interacting matter which is produced in high-energy heavy-ion collisions. Insights on non-perturbative QCD are also provided [34].

The necessity to subtract the large combinatorial background coming from semi-muonic decays of pions and kaons to properly identify low-mass dimuon spectra represents a challenging task. The MFT will significantly improve the performance of ALICE for the measurement of dimuons at forward rapidities, along with an improved mass resolution. The measurements of low-mass dileptons will also profit from an improved vertex resolution and from a higher rate that will increase the number of events in the central barrel by a factor of 100.

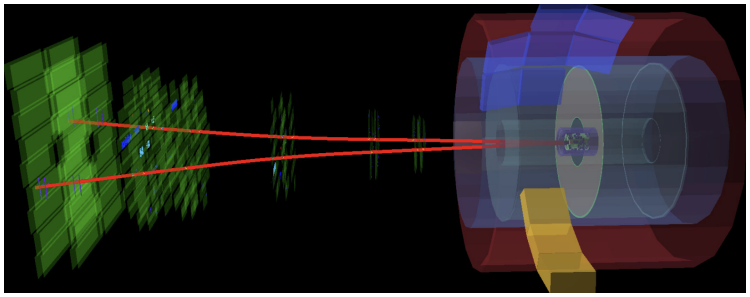

Fig. 3.5: Event display of a candidate event for vector meson photoproduction at forward rapidity.

Photoproduction of vector mesons will be further described in the next sections.

3.4 UPC: recent measurements and prospects

Hadrons accelerated in colliders such as the LHC carry a strong electromagnetic field. Their electric and magnetic fields being perpendicular to the motion of the particles may be treated as a flux of nearly real photons. These photon fields can give rise to photonuclear (photon-ion) or purely electromagnetic two-photon interactions in ultra-peripheral collisions (UPC) [35]. Using these processes, we are offered a way to study the fundamental QED and QCD interactions.

When charged hadrons collide at large impact parameters way beyond the range of the strong force, the interaction via the strong force is suppressed. The hadrons can, however, interact electromagnetically, in a photoproduction process, where a set of virtual photons is exchanged between the hadrons.

Vector meson photoproduction in UPC can be characterised by a very clean signature in the detector: two or four tracks, from the decay of a vector meson, in an otherwise empty detector. An example of a candidate event for vector meson photoproduction at forward rapidity can be seen in Fig. 3.5.

3.4.1 Ultra-peripheral Pb–Pb collisions

In a **photonuclear** process, a photon can interact either with the whole nucleus or with a single nucleon only. If the photon interacts coherently with the whole nucleus, in a process called coherent production, the transverse momentum of the produced di-lepton or vector meson is constrained by the radius of the lead nucleus to $p_T \sim 60$ MeV/c. The other possible process is an incoherent production, where the photon interacts with a single nucleon only. This

process is characterised by a larger transverse momentum of a few hundreds of MeV/c.

A photon emitted by one nucleus fluctuates to a quark-antiquark dipole, which then scatters elastically from the other nucleus emerging as a real vector meson. The scattering occurs through Pomeron exchange, where the photon quantum numbers are preserved. In perturbative QCD, Pomerons are made up of gluons, so the process is sensitive to the gluon distribution in the target nucleus.

In Pb–Pb collisions, the differential cross section for vector meson production can be calculated as a product of the photon flux $N_{\gamma/\mathrm{Pb}}$ and the corresponding photoproduction cross section $\sigma_{\gamma\mathrm{Pb}}$. Both ions can serve as a source of photons, therefore the cross section σ_{PbPb} is given by a sum of two terms

$$\frac{d\sigma_{\mathrm{PbPb}}(y)}{dy} = N_{\gamma/\mathrm{Pb}}(y, M)\sigma_{\gamma\mathrm{Pb}}(y) + N_{\gamma/\mathrm{Pb}}(-y, M)\sigma_{\gamma\mathrm{Pb}}(-y), \tag{3.3}$$

where M and y are the mass and rapidity of the produced vector meson, respectively.

The photoproduction cross sections $\sigma_{\gamma\mathrm{Pb}}(y)$ and $\sigma_{\gamma\mathrm{Pb}}(-y)$ could be decoupled by measuring the vector meson production in UPC with and without additional activity in ZDC.

In a two-photon interaction, the two electromagnetic fields collide and by coupling the fields to any particles that carry charge, a wide variety of final states is created. For relativistic nuclei, the configuration may be represented as a flux of photons following the Weizsacker-Williams approach [36].

The photon number density[2] $N(k, b)$ at an impact parameter b from a relativistic heavy-ion with charge Z and Lorentz boost γ is given by

$$N(k, b) = \frac{Z^2\alpha}{\pi^2}\frac{k}{(\hbar c)^2}\frac{1}{\gamma^2}\left[K_1^2(x) + \frac{1}{\gamma^2}K_0^2(x)\right], \tag{3.4}$$

where k is the photon energy, $x = kb/\gamma\hbar c$, $\alpha \approx 1/137$ the electromagnetic fine structure constant, and K_1 and K_0 are modified Bessel functions.

For relativistic heavy ions, the first term in Eq. (3.4) dominates, so it is the only one considered further. This first term gives the flux of transversely polarized photons.

There are several models based on 3.3 that predict the cross section for photonuclear processes. A model by Klein and Nystrand implemented in the STARlight Monte Carlo generator [37] is used in this work.

[2]number of photons per unit area, per unit energy

Coherent vector meson production

In the STARlight framework [37], the cross sections for coherent production on nuclear targets are determined using a classical Glauber calculation

$$\sigma(AA \to AAV) = 2 \int dk \frac{dN_\gamma(k)}{dk} \sigma(\gamma A \to VA) = \\ = 2 \int_0^\infty dk \frac{dN_\gamma(k)}{dk} \int_{t_{\min}}^\infty dt \frac{d\sigma(\gamma A \to VA)}{dt}\bigg|_{t=0} |F(t)|^2 \quad (3.5)$$

where $F(t)$ is the nuclear form factor.

Given the condition that the two nuclei do not interact hadronically, the photon flux $dN_\gamma(k)/dk$ is calculated by integrating Eq. (3.4) over impact parameter space. For each impact parameter, the photon flux striking the nucleus is determined and spread evenly over the nucleus.

The calculation of the cross section can be done assuming narrow or wide resonance. For the ρ^0 meson, the difference is quite significant: the cross section in heavy-ion collisions is reduced by about 5% with a wide resonance used.

ρ^0 meson photoproduction from ultra-peripheral Pb–Pb collisions: recent results

Performance studies of UPC using the MFT for Run 3 can be found in Chapter 5. Let us summarise the recent ALICE measurements first.

ALICE has reported results on coherent ρ^0 photoproduction from ultra-peripheral Pb–Pb collisions at $\sqrt{s_{NN}} = 2.76$ from 2011 data [38], see Fig. 3.6 and 3.7. The measured cross section was found to be in agreement with both STARlight and the Goncalves and Machado (GM) model. The prediction by Glauber–Donnachie–Landshoff (GDL) is about a factor 2 larger than in data. This confirmed the STAR findings.

The rapidity dependance of the coherent ρ^0 production cross section in Pb–Pb UPC at $\sqrt{s_{\rm NN}} = 5.02$ TeV has recently been published [39]. The mass and width has been shown to be compatible with PDG: $m = 769.5 \pm 1.2(\text{stat.}) \pm 2.0(\text{syst.})$ MeV/c^2, $\Gamma = 156 \pm 2(\text{stat.}) \pm 3(\text{syst.})$ MeV/c^2, see Fig. 3.8.

The measurements of coherent ρ^0 photoproduction were shown to be in good agreement with models following the parton-based colour-dipole approach and with the Gribov-Glauber shadowing framework, see Fig. 3.9.

Recently, the first measurement of the coherent photoproduction of ρ^0 vector mesons in Xe–Xe collisions at $\sqrt{\rm s_{NN}} = 5.44$TeV [40]. The invariant mass in Fig. 3.10 was fitted by a Breit-Wigner resonance with a continuum term. The fair agreement between data and predictions suggest that this process is well understood within the current experimental uncertainties. This paper

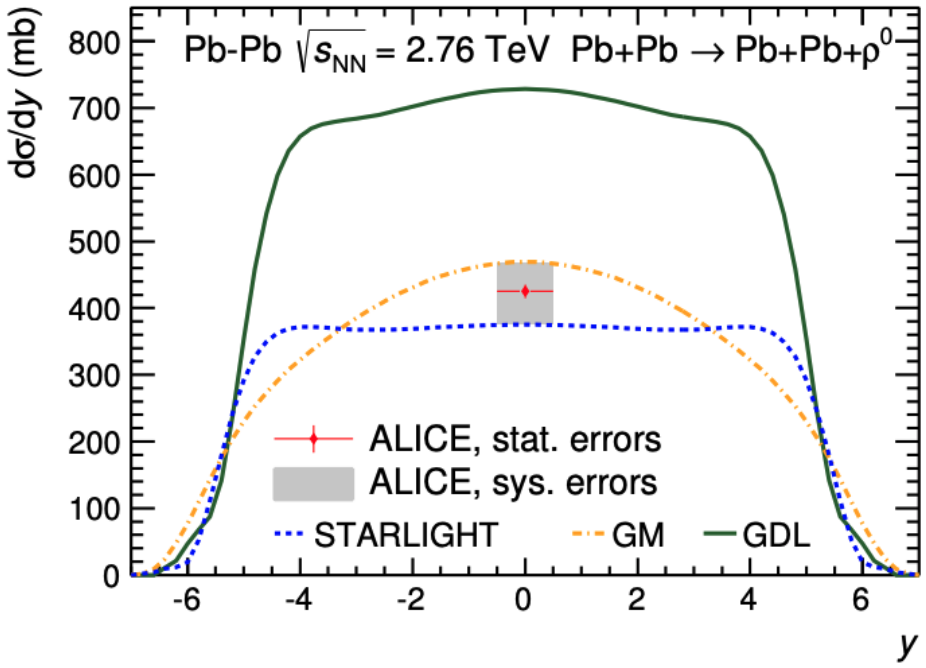

Fig. 3.6: The cross section for coherent ρ^0 photoproduction in UPC for the three models compared with the ALICE result [38].

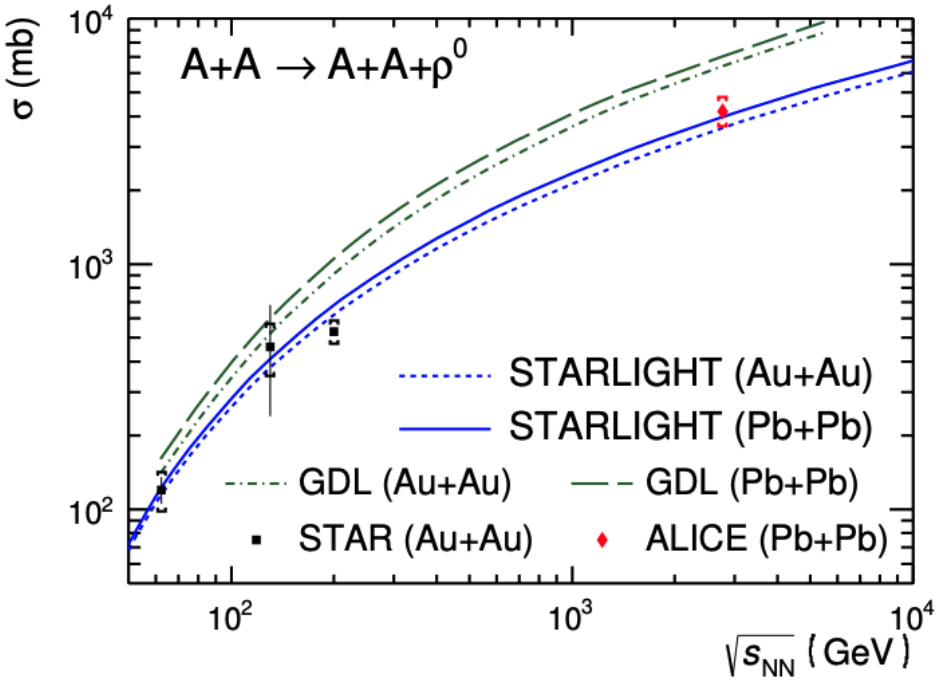

Fig. 3.7: Excitation function for coherent and exclusive ρ^0 production with results from ALICE and STAR included [38].

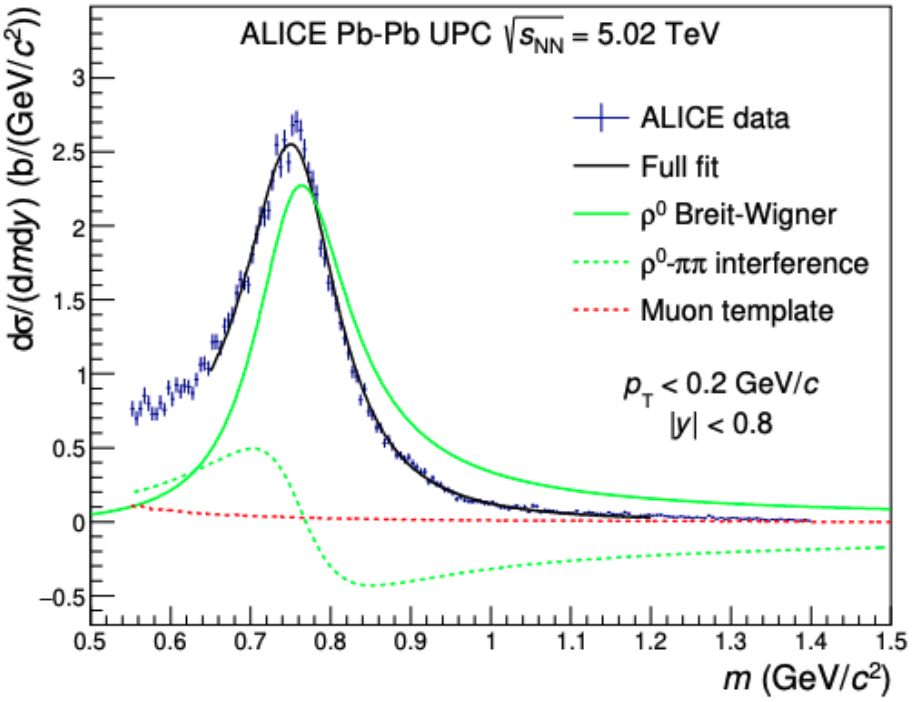

Fig. 3.8: Invariant mass distribution of pion pairs [39].

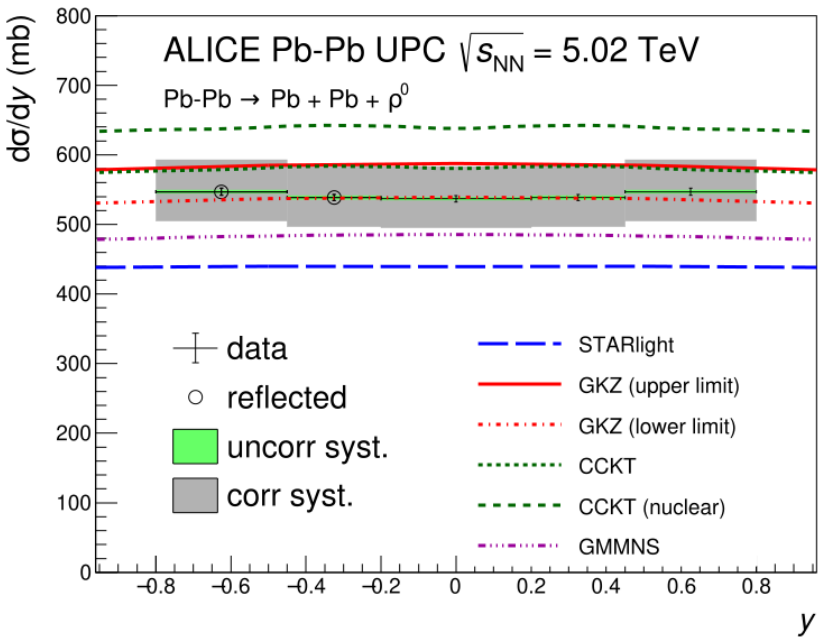

Fig. 3.9: Cross section for the coherent photoproduction of ρ^0 vector mesons in Pb–Pb UPC as a function of rapidity with the predictions of the different models [39].

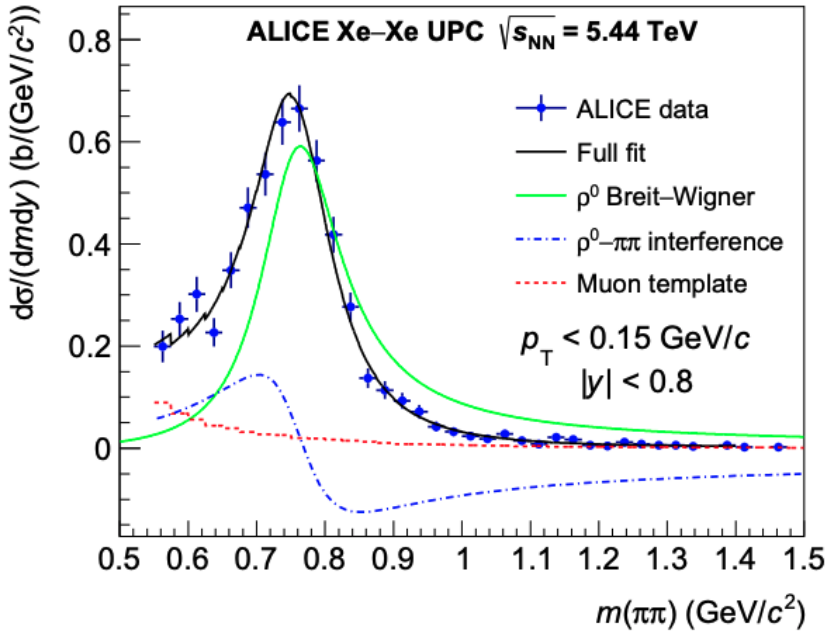

Fig. 3.10: Invariant mass distribution of pion pairs with different components [40].

provided the first study of the atomic number (A) dependence of the cross section for the coherent ρ^0 photoproduction, which is particularly sensitive to nuclear shadowing effects. It was found to be consistent with a power-law behaviour with a slope of 0.96 ± 0.02, see Fig. 3.11. The A dependence of the cross section is a strong indicator of the importance of QCD effects.

All the measurements were performed at midrapidities: there are no previous measurements at rapidites covered by the MFT, which motivates our studies of MFT performance for the measurement of UPC in Run 3.

3.4.2 UPC prospects with ALICE for Run 3

In Run 3 with ALICE, the full delivered luminosity can be essentially integrated without significant trigger or dead-time inefficiencies, thanks to continuous readout, see Sec. 1.3.1. Tracking efficiency and geometrical acceptance is determined by the ITS, MFT, TPC and the Muon Spectrometer. Final-state neutron emission in UPC events can be detected by the ZDC and vetoes can be imposed using the FIT system.

The expected physics reach can be estimated from the number of vector mesons expected in the upcoming LHC runs. The expected cross sections and vector meson yields for six representative vector meson decays including the decay branching ratios are shown in Table 3.1. The rates were calculated

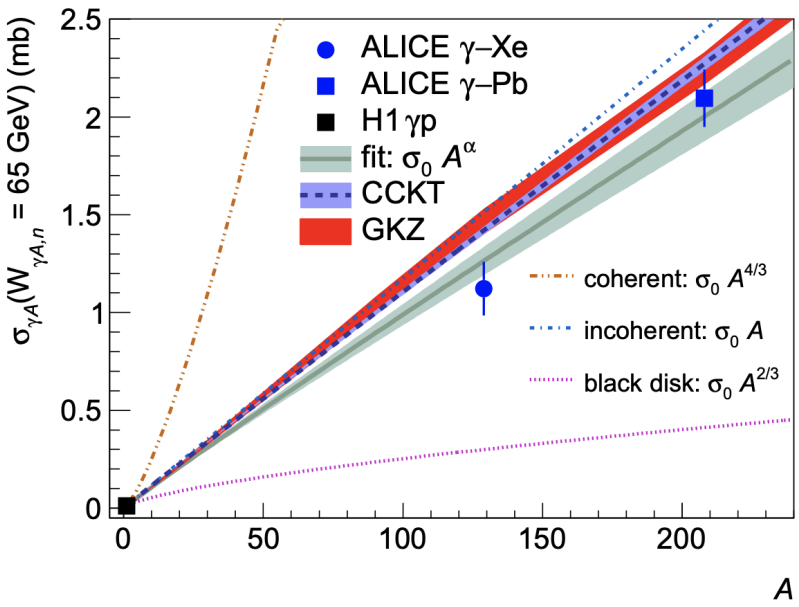

Fig. 3.11: The dependence of the γA cross section for the coherent production of the ρ^0 meson and the corresponding power-law fit shown [40].

using the STARlight generator [37]. For forward rapidites covered by the MFT, there are several billions of $\rho \to \pi^+\pi^-$ expected. The studies conducted in Chapter 5 address a question if they can be measured by the MFT as a standalone detector.

PbPb						
meson	σ	all	$\lvert y\rvert < 0.9$	$\lvert y\rvert < 2.4$	$2.5 < y < 4.0$	$2 < y < 5$
		#events	#events	#events	#events	#events
$\rho \to \pi^+\pi^-$	5.2 b	68B	5.5B	21B	4.9B	13B
$\rho' \to \pi^+\pi^-\pi^+\pi^-$	730 mb	9.5B	210M	2.5B	190M	1.2B
$\phi \to \mathrm{K}^+\mathrm{K}^-$	0.22 b	2.9B	82M	490M	15M	330M
$\mathrm{J}/\psi \to \mu^+\mu^-$	1.0 mb	14M	1.1M	5.7M	600K	1.6M
$\psi(2\,\mathrm{S}) \to \mu^+\mu^-$	30 μb	400K	35K	180K	19K	47K
$\Upsilon(1\,\mathrm{S}) \to \mu^+\mu^-$	2.0 μb	26K	2.8K	14K	880	2.0K

Table 3.1: Cross sections and numbers of events in 13 nb^{-1} integrated luminosity for vector mesons in Pb–Pb collisions, where B, M and K denote $10^9, 10^6, 10^3$ respectively. Rates and cross sections include the relevant branching ratios. Taken from [27].

Chapter 4

Commissioning of MFT ladders

With the LHC schedule available at the beginning of the author's work on the MFT, the LS2 was foreseen to occur until 2020. In the meanwhile, the LS2 schedule has suffered modifications [41]: 2021 is mainly dedicated to hardware commissioning, commissioning with beam is expected in the beginning of 2022 and the data taking will start in April 2022.

The major part of the author's work at CERN has been already covered in [21], which included the work on the ladder assembly and qualification procedures. The fundamental principles for understanding the behaviour of the ladders were presented.

The following sections focus on the extensive description of the main steps of the qualification procedures and the requirements for different results of the qualification. The qualification process in a similar form will be repeated after the installation of the detector in the ALICE cavern.

4.1 Hybrid Integrated Circuit and Ladder Assembly

The main requirements for the ladder assembly are a reliable high-quality technique to connect the pixel chips to the FPC and a placement accuracy of each chip of the order of μm.

A system called ALICIA, also called MAM (Module Assembly Machine), captured in Fig. 4.1, is used for an automated inspection and assembly of chips on an FPC. The chip quality (dimensions inspection, edge integrity, and pad cleanliness) is inspected by the high resolution vision system. To give ALICE the required accuracy, ALICIA uses a high-accuracy (< 0.1 μm) image system. In the final assembly, the accuracy of < 5 μm over the full array of chips is achieved.

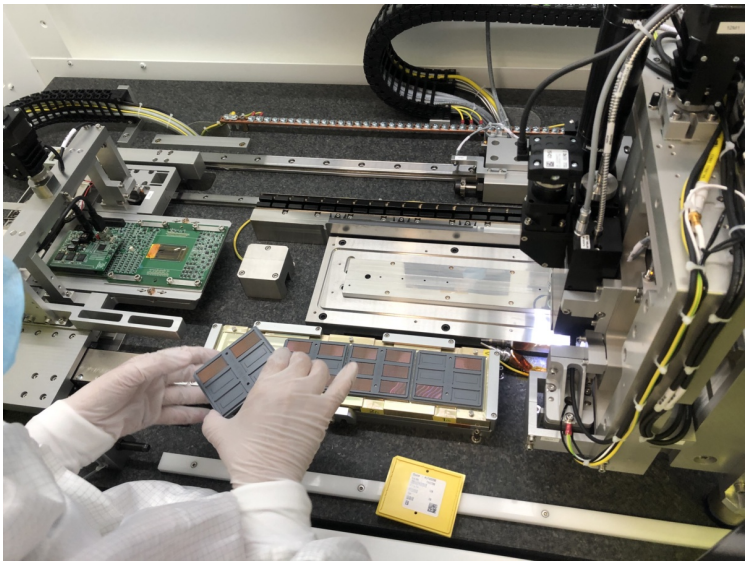

Fig. 4.1: Chips positioning in the ALICIA machine in a cleanroom at the Department Silicon Facility (DSF) at CERN. After being picked from the wafer, chips are stored in trays. A combination of chips satisfying the desired qualification result is chosen for ladder assembly.

After the chips were inspected and positioned using a vacuum gripper, they are glued to the FPC. After the glue polymerisation, the HIC is placed in the wire bonding machine. Wire bonds are interconnections between the FPC and chips made with a 25 μm wire. Three wire bonds per pad are created. Once bonded, a HIC becomes a ladder.

Performing the steps mentioned above makes the ladder prepared for the qualification tests.

4.2 Ladder quality assurance

Ladder qualification is a crucial tool in the process of building the MFT detector.

A visual inspection is carried out to reveal any mechanical damage that could have been inflicted during the assembly.

The qualification process consists of several stages: electrical tests, following a similar, although more light-weight procedure as the single chip tests, functional tests, and eye measurement.

The whole qualification is first performed with $V_{\mathrm{BB}} = 0$ V and then repeated at $V_{\mathrm{BB}} = -3$ V.

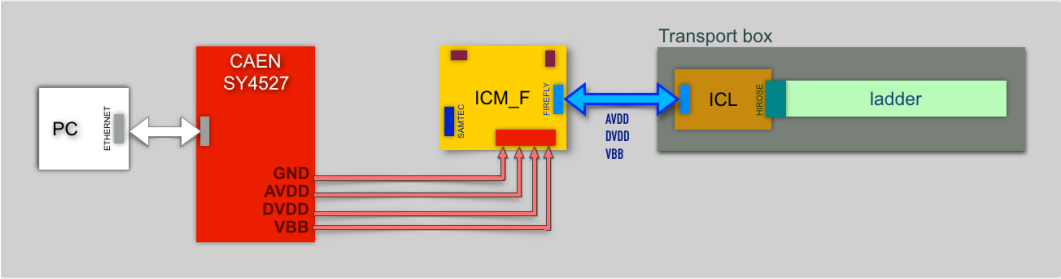

Fig. 4.2: Test bench used for the smoke test.

4.2.1 Smoke test

The term *smoke test* refers to a test when the ladder, or generally a circuit, is attached to power for the first time, which could, in some cases, actually produce smoke, which would mean that the circuit is faulty and there is no need to do more testing.

To perform the smoke test and the following tests, the ladder is connected to an ICL card (*Intermediate Card for Ladder*), which provides an electrical interface between the ladder and the test-bench read-out, see Fig. 4.2.

A maximum voltage of 1.8 V is set for `AVDD` and `DVDD`; for back-bias the voltage is set to $V_{\mathrm{BB}} = -3$ V. In the smoke test, the power is ramped up gradually via a remotely controlled system. This is very useful to spot short circuits and transient overcurrents that stabilise and allow for further operation. Any eventual abnormalities in the current can be visually noticed in the GUI, which results in aborting all tests and there is an extra intervention required to fix the eventual problems.

4.2.2 Electrical tests

Electrical tests consist of three parts. In the first part, called `test A`, the power is sent to the ladder and the total power consumption of the ladder is tested. With both `AVDD` and `DVDD` fixed at 1.8 V, the current consumption is noted. In the `test B`, the clock signal is also sent to ladder. Finally, `test C` applies power, clock as well as activity on all chips. The `test C` therefore represents a simultaneous digital scan on all working chips.

4.2.3 Ladder functional tests

The power supply used for the functional tests provides a voltage of 5 V. However, the operating voltage of the ALPIDE chip is only 1.8 V, so there is a power converter used for the transition between these two voltages.

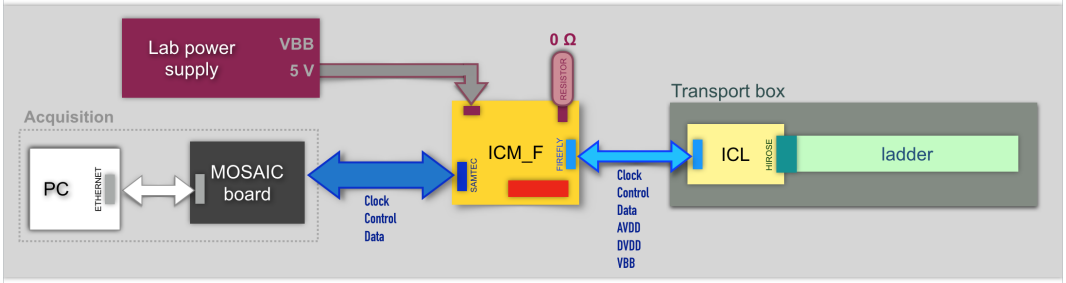

Fig. 4.3: Test bench hardware for functional tests without back-bias voltage: $V_{\mathrm{BB}} = 0$ V.

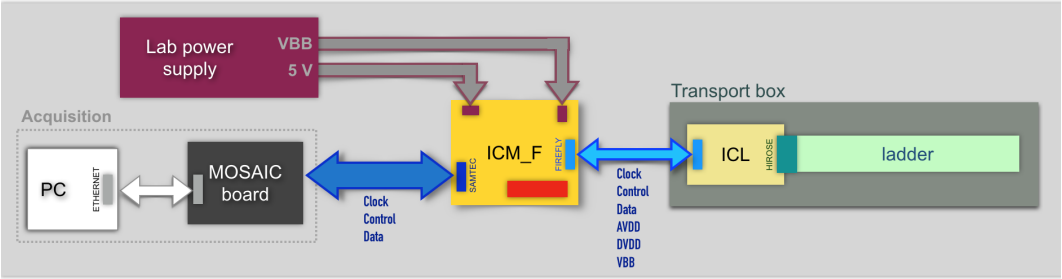

Fig. 4.4: Test bench hardware for functional tests with the back-bias voltage set to $V_{\mathrm{BB}} = -3$ V.

All functional tests are done on the test benches without back-bias voltage ($V_{\mathrm{BB}} = 0$ V) and with back-bias ($V_{\mathrm{BB}} = -3$ V), where the 0 Ω resistor terminator in the `ICM_F` board is replaced by a negative potential supplied by the laboratory power supply, see Fig. 4.3 and 4.4. The `ICM` (Intermediate Card for MOSAIC) represents an adaptation board providing power regulation and data connector adaptation to the MOSAIC data acquisition system.

A 5 V voltage is delivered for the analog and digital voltages from the laboratory power supply. An ICL card is used to provide the power for the ladder and to send the data to the MOSAIC board [42], which is used for testing the configuration and read-out that conducts the measurements on the chip commanded by the computer. ALPIDE testing software [43] is used to control the tests via the GUI window and to gather the results.

Read-out test

The read-out test checks the reading/writing configuration (I/O connection) and writing to the chips' registers, where the clock is active and provided to all chips. The read-out test, executed by the software prior to all other functional tests, verifies only the slow control circuitry of the chip, the digital and analog parts are not tested here.

If any chip in the ladder is found to be not responding, there is an option to disable it and proceed with the functional tests for all other enabled chips.

FIFO scan

An ALPIDE chip contains around 100 registers: small blocks of memory allocated for a particular task, mostly used to save variables and data. A FIFO (*first in, first out*) test is a simple test checking the registers if they are storing the data in the right way, that is the first (oldest) entry is processed first.

A sequence of bits is sent to the the register if it is available for the write and read actions. After a while, the read-out of the register is performed to see if the sequence differs from or corresponds to the initial one.

There are two possible results of the test: GOLD and RED, where two or more errors in the FIFO test result in RED. All ladders with the RED results are considered non-conformal.

Digital scan

A digital scan tests the behaviour of the digital part of the chip. Using a test pulse pattern, each pixel is pulsed 50 times. In this manner, dead, inefficient and noisy pixels are detected:

- if a pixel does not respond at all, it is considered **dead**,
- if a pixel responds at least one time but less than 50, it is considered **inefficient**,
- if a pixel responds *more* than 50 times, it is considered **noisy**.

Therefore, only the pixels from which we get exactly 50 responses are considered conformal. If we label the dead, inefficient and noisy pixels as *faulty* pixels, the outcome of the digital scan results from the number of faulty pixels n_f out of the total 512×10254 pixels in a chip:

- $0 \leq n_f < 50 \Rightarrow$ GOLD,
- $50 \leq n_f < 2100 \Rightarrow$ SILVER,
- $2100 \leq n_f < 5243 \Rightarrow$ BRONZE,
- $n_f \geq 5243 \Rightarrow$ RED.

Ladders with GOLD, SILVER, and BRONZE results of the digital scan are marked conformal.

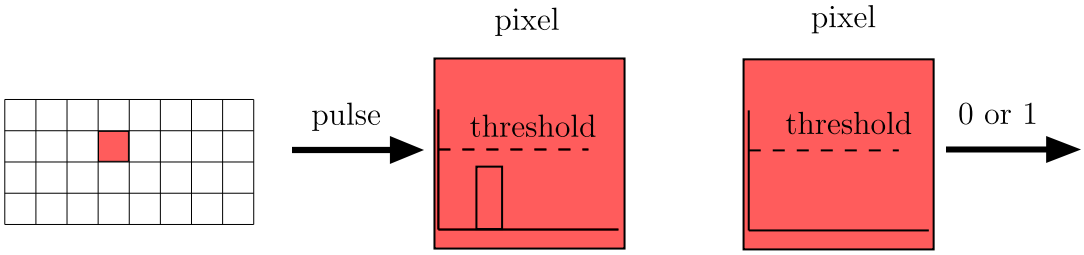

Fig. 4.5: An overview of the steps performed by a threshold test: a pixel is selected, while the rest of the chip is masked. A pulse is injected into the pixel and finally, the value in pixel's memory is read.

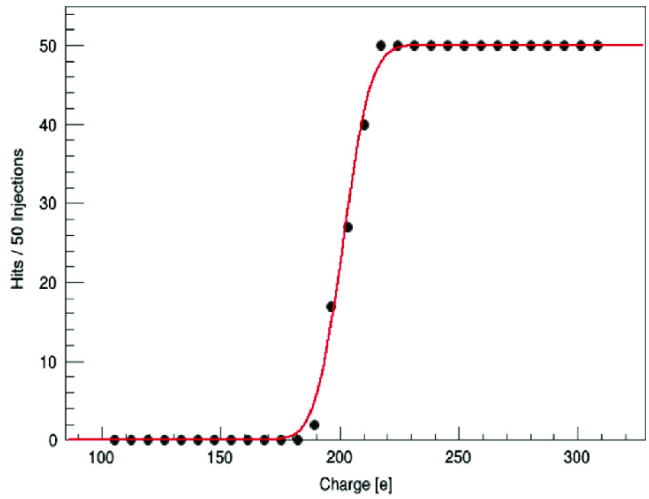

Fig. 4.6: A threshold S-curve for the front-end pixel chip. The input level of electrons of the injected pulse is plotted against the number of hits detected in the pixel out of 50 measurements. The threshold can be seen as the number of electrons where the number of hits reaches 50%. Taken from [44].

Threshold scan

The stages of the threshold scan are illustrated in Fig. 4.5. After a specific pixel was selected and the rest were masked, an analog pulse resembling a particle hit is injected into the pixel. The height of the pulse is an analogue to the energy deposited by the particle.

The value of the injected charge at which the pixel starts to detect particles is extracted as a result of the threshold scan. An increasing charge q_{inj} is injected $N_{\text{inj}} = 50$ times through the injection capacitance C_{inj}. The results are fitted with the following function

$$f\left(q_{\text{inj}}\right) = \frac{1}{2} N_{\text{inj}} \left[1 + \text{erf}\left(\frac{q_{\text{inj}} - q_{\text{thr}}}{\sqrt{2\sigma}}\right)\right], \tag{4.1}$$

where q_{thr} is treated as the threshold (the charge at which a selected pixel registers a hit with a probability of 50%), σ is a parameter accounting for the noise, which manifests in the slope of the function[1], see Fig. 4.6. The noise is defined as the difference in DAC levels where the probability is 10% and 90%.

The threshold value varies from pixel to another. The test therefore needs to be performed for multiple pixels. After the threshold is obtained for each pixel in the selection, a histogram is created thus a distribution of threshold and noise for each chip in the ladder is created, see Fig. 4.7.

Generally, the threshold and noise mainly depend on the `ITHR` and `VCASN` values of the pixel. The value of the threshold is approximately linearly increasing proportionally to the `ITHR` value. For the `VCASN` value, the situation is the opposite: the threshold decreases with increasing `VCASN`. In the tuned threshold scan, both parameters are set such that all pixels in the matrix have a uniform threshold value [24].

Similarly to the digital scan, ladders are ranked according to the number of faulty pixels. If the threshold is unrealistically high, we can detect a *dead* pixel. In the same way, if the threshold of a pixel is 0, we can assume a *stuck* pixel. Ladders with the RED result of the threshold scan are treated as non-conformal.

Noise occupancy scan

The noise occupancy scan is performed to obtain a fake hit rate, which describes the probability of registering a hit by a pixel when there was no ionising particle passing through the pixel. The noise occupancy is defined as the number of pixels producing a fake hit divided by the total number of pixels in the chip. The ALICE upgrade plans [17] require a noise occupancy below 10^{-5} hits/event/pixel, corresponding to about 5 fake hits per event per chip.

[1] The noise is modeled by the standard deviation of the derivative of $f\left(q_{\text{inj}}\right)$.

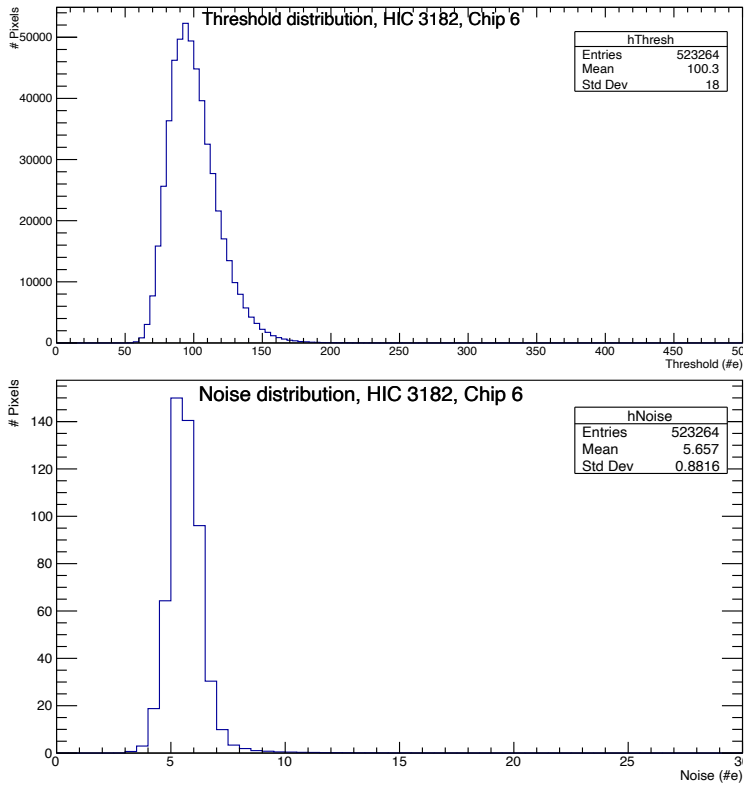

Fig. 4.7: Result of the threshold scan for chip 6 in ladder HIC_3182.

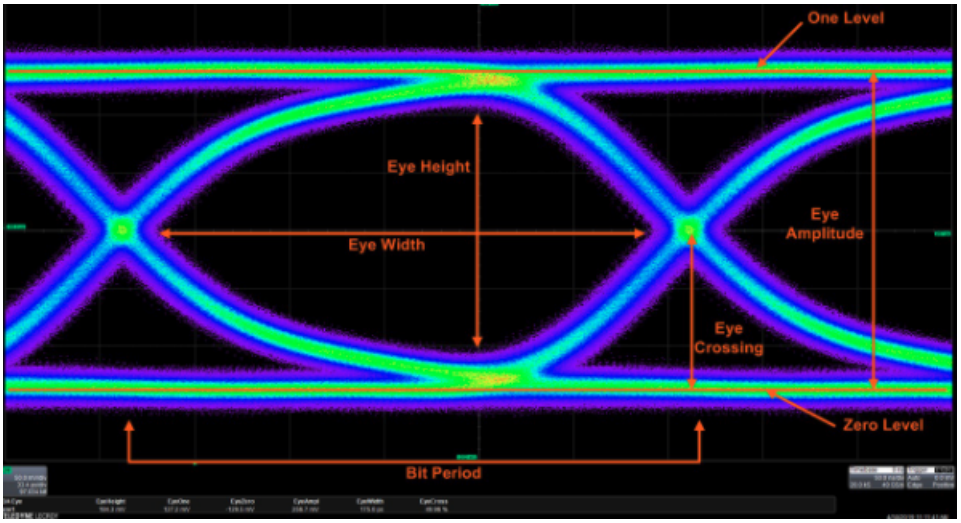

Fig. 4.8: The main measurement parameters associated with eye diagrams [45].

In the noise occupancy test, a large number of random triggers from the MOSAIC board is produced and the number of registered hits is then read by the board. Most of the noise is produced by the so-called *hot* pixels: pixels with an increased probability of producing a hit in comparison to the rest of the pixels. Masking a small number of pixels can significantly reduce the fake-hit rate.

Eye measurement

Measuring the eye diagram is a general-purpose tool for analysing digital signals. In an oscilloscope, an eye diagram is formed by overlaying multiple single clock periods. In the days of analog oscilloscopes, the eye diagram was formed by triggering the oscilloscope with the serial data clock and acquiring multiple bits over time using storage display. Digital oscilloscopes form the eye by acquiring very long records with many serial bits. A more quantitative evaluation of the eye opening can be obtained using eye measurement parameters as shown in Fig. 4.8.

The eye amplitude, a measure of the overall amplitude of the eye, is based on the difference between the mean of the one level and the mean of the zero level. A measurement of the vertical eye opening, the eye height, represents a determination of the signal-to-noise ratio, starting with the difference of the mean of the one level and mean zero level and then subtracting the standard deviation of both levels.

The eye width gives an indication of the total horizontal jitter in the signal. Like the eye height, the width measurement is statistical in nature.

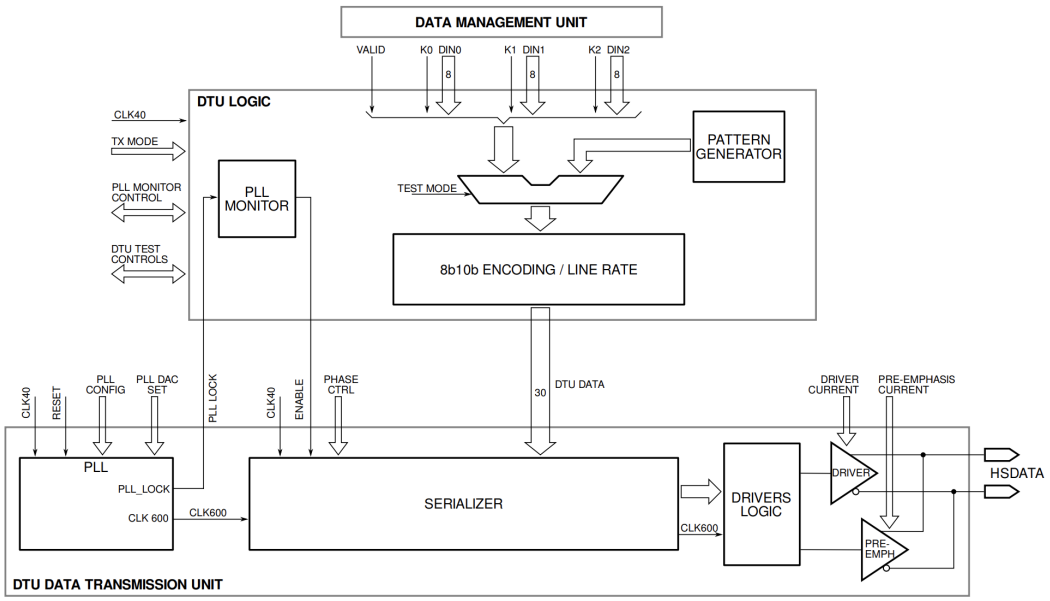

Fig. 4.9: Functional block diagram of the Data Transmission Unit and the related digital module DTU logic [46].

The eye crossing is the amplitude point where the rising and falling edges intersect. An ideal eye diagram would have crossings at 50% of the amplitude.

When testing the ALPIDE sensors used in the MFT, after obtaining a digital waveform, the parts of the waveform corresponding to each individual bit are folded into a single graph. A resulting plot is made with multiple samples of the waveform, representing the average statistics of the signal shape, see Fig. 4.10. During the measurement, the sensor is put in the PRBS (pseudo-random bit sequence) mode, where the Data Transmission Unit (DTU) sends a pseudo-random sequence of bits for off-chip processing.

In the MFT, the eye scan functionality is based on the comparison between the *data sample* in the nominal centre of the eye and the *offset sample* captured by the same circuitry at a programmable horizontal and vertical offset from the nominal centre. A bit error, defined as a disagreement between the two samples, is used to calculate the Bit Error Rate (BER), the ratio of bit errors to the total number of comparisons at a particular horizontal and vertical offset. The calculation of BER at each possible offset provided the data for the statistical eye diagram. The colours in Fig. 4.10 are mapped to the value of the BER.

The architecture of the DTU in an ALPIDE sensor is shown in Fig. 4.9. High speed data transmission (1.2 Gbit/s) is programmed in the functional block responsible for the serialisation of the data. Three parameters involved in the same functional block, the PLL Charge Pump (CP), the DTU driver (D)

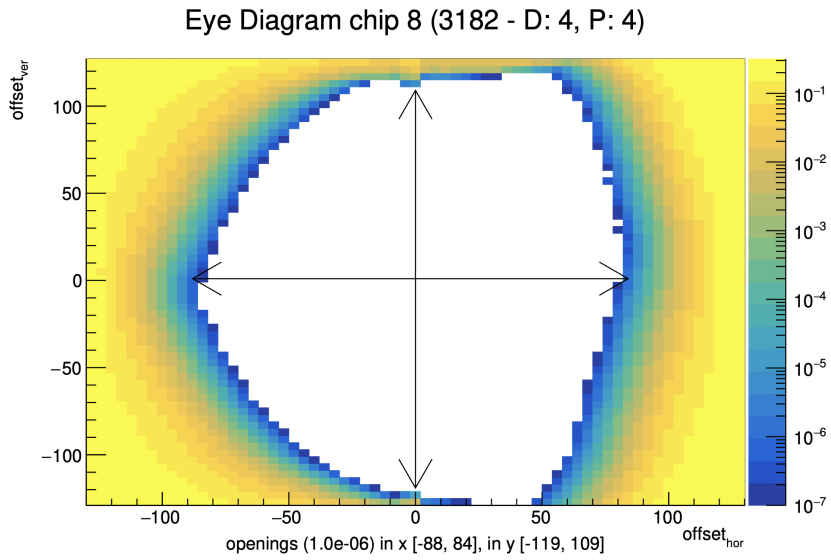

Fig. 4.10: Measured eye diagram for chip 8 in ladder HIC_3182.

and the DTU Pre-Emphasis (P), affect the results of the Eye Diagram. During the functional tests of the MFT half-disks, two sets of parameters have been used: $D = 4, P = 4, CP = 8$ and $D = 4, P = 10, CP = 10$, where the latter set produced significantly better results of the eye diagrams.

The eye diagram qualification system is different compared to other tests. There are certain criteria for BER `X opening` and `Y opening`, the diagrams are evaluated and graded Gold, Silver, Bronze, and Red. Possible ranges are reported in [24], ladders with RED result of the eye measurement are considered non-conformal.

4.3 Ladder qualification analysis

The following sections summarise the main interpretations of the analysis of the ladder qualification programme of all produced ladders for the MFT; a more extensive description can be found in the author's previous work [21].

4.3.1 Yield of conformal ladders

This analysis is based on the data from the 528 ladders that have been assembled and qualified afterwards. All plots consider only conformal ladders, the criteria to mark a ladder as conformal ensuing qualification tests were presented above. The total number of conformal ladders is summarised in Table 4.1. We can see that majority of the produced ladders have been declared

LADDERS	2-chip	3-chip	4-chip	5-chip
total amount	57	236	158	21
conformal amount	45	176	134	18
conformal yield	79%	75%	85%	86%

Table 4.1: Summary of the amount of produced and bonded ladders and the yield of the conformal ones.

conformal, which is, given the complexity of the assembly process, a satisfactory result. There are various reasons why a ladder could have been declared not conformal, e.g., a large number of dead pixels or communication problems resulting in a problematic eye diagram.

4.3.2 Power consumption

Electrical tests, consisting of `test, A, B` and `C`, were analysed to explore the power consumption of the ladders, see Fig. 4.11. All the plots were normalised by the number of chips in the ladder. After applying the back-bias voltage $V_{\mathrm{BB}} = -3$ V, a current IBB of 7.7 mA was measured for the majority of ladders, with the acceptability criteria being IBB < 10 mA.

4.3.3 Threshold-noise characteristics

The threshold and noise distributions for ALPIDE chips in all types of ladders (2-, 3-, 4- and 5-chip ladders) were plotted. At first separately; after the same behaviour for all types was observed, the plots were merged and values for single chips were plotted. These include threshold mean, threshold deviation, noise mean, noise deviation, all with and without back-bias voltage $V_{\mathrm{bb}} = -3$ V.

As can be seen in Fig. 4.12, the threshold is uniform across different sensors as expected. We observe peaks at 100 electrons both for $V_{\mathrm{BB}} = 0$ V and $V_{\mathrm{BB}} = -3$ V: the goal of uniform threshold was achieved. In the distribution with back-bias voltage, some chips with a threshold below 100 electrons occurred. For average noise, the most frequent values are ~ 6 electrons, applying the back-bias voltage lowers the average noise to ~ 4 electrons.

Threshold and noise RMS distributions can be found in [21].

It was shown that applying back-bias voltage reduces the noise and makes the threshold distribution more narrow, which is expected since the back-bias increases the depletion zone and therefore improves the S/B ratio of the charge collection diode.

4.4 Dead and noisy pixels

The analysis to find the dead and noisy pixels has been done separately for the values obtained from the digital scan and the threshold scan.

Data for dead pixels in a chip are plotted in Fig. 4.13. The highest peak is observed in the first bin, which is a satisfactory result, as it corresponds to no dead pixels present in the sensor. Another peak can be seen at 512 pixels, which corresponds to one full row, around 1024 and 2048 pixels, which could be explained by one full column or double column of dead pixels respectively. There are no major differences between the number of dead pixels measured with $V_{\mathrm{BB}} = 0$ V or with $V_{\mathrm{BB}} = -3$ V in both the digital and threshold scan.

Considering the number of noisy pixels, the result is satisfactory: a peak at zero is observed and there is a negligible number of ladders with more noisy pixels present.

4.5 Full MFT assembly and installation

The disk supports made from plastic and heat exchangers with all their components have been designed in SUBATECH in Nantes, France. The heat exchanger is made of a sandwich of two carbon composite cold plates, embedded polyimide pipes with 1 mm in diameter and a rigid foam in between. Tested ladders were glued to the half-disks and the qualification procedure was repeated and reported internally in ALICE. According to the results of the qualification of the assembled detector, 99% of the detector has an active surface and only 0.05% of the pixels will have to be masked. The signal quality obtained from the eye measurement with the tuned parameters is excellent. It has also been shown that MFT can run with a uniform threshold of 100 electrons.

The half-MFT assembly at CERN proceeds in two steps, first the assembly inside the MFT cone, then the assembly of the MFT cone inside the barrel. Each step starts with servicing with cables for both signals and power as well as pipes for cooling. Once all five half-disks are installed, a qualification test is performed for about one week, which puts the survey of the disks to an end.

To assemble the MFT cone with the barrel (see Fig. 4.14), the MFT half-cone needs to get mechanically fixed inside the barrel, which is followed by the connection of the cables and cooling tubes to the MFT read-out board and a qualification test of the global assembly is performed for at least 3 months.

The installation and commissioning in ALICE cavern follows. The MFT has been installed in ALICE cavern in December 2020, as pictured in Fig. 4.15 and 4.16. Full commissioning of the installed detector includes full DTU scan for optimisation, measuring eye diagrams with more points, noise occupancy scan and threshold scans.

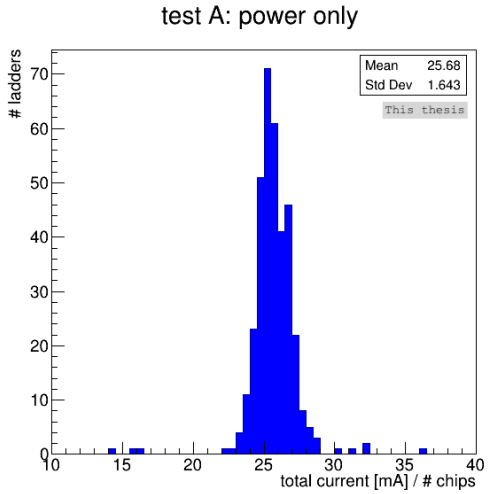

(a)

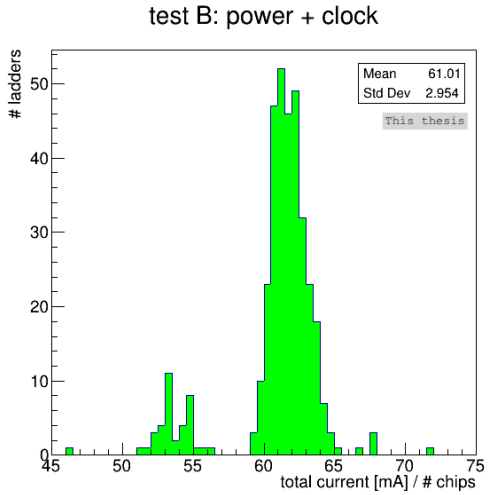

(b)

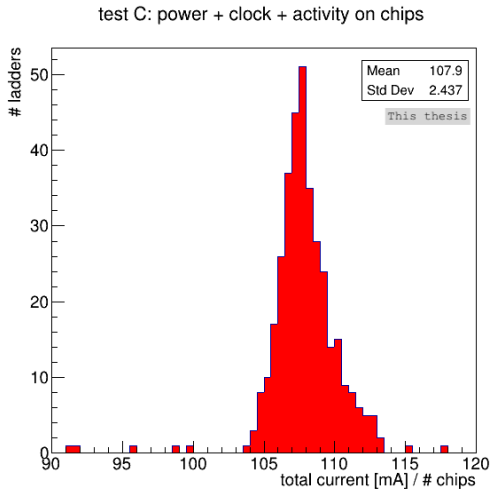

(c)

Fig. 4.11: Results of electrical test: Power consumption of ladders is electrical tests A, B, and C.

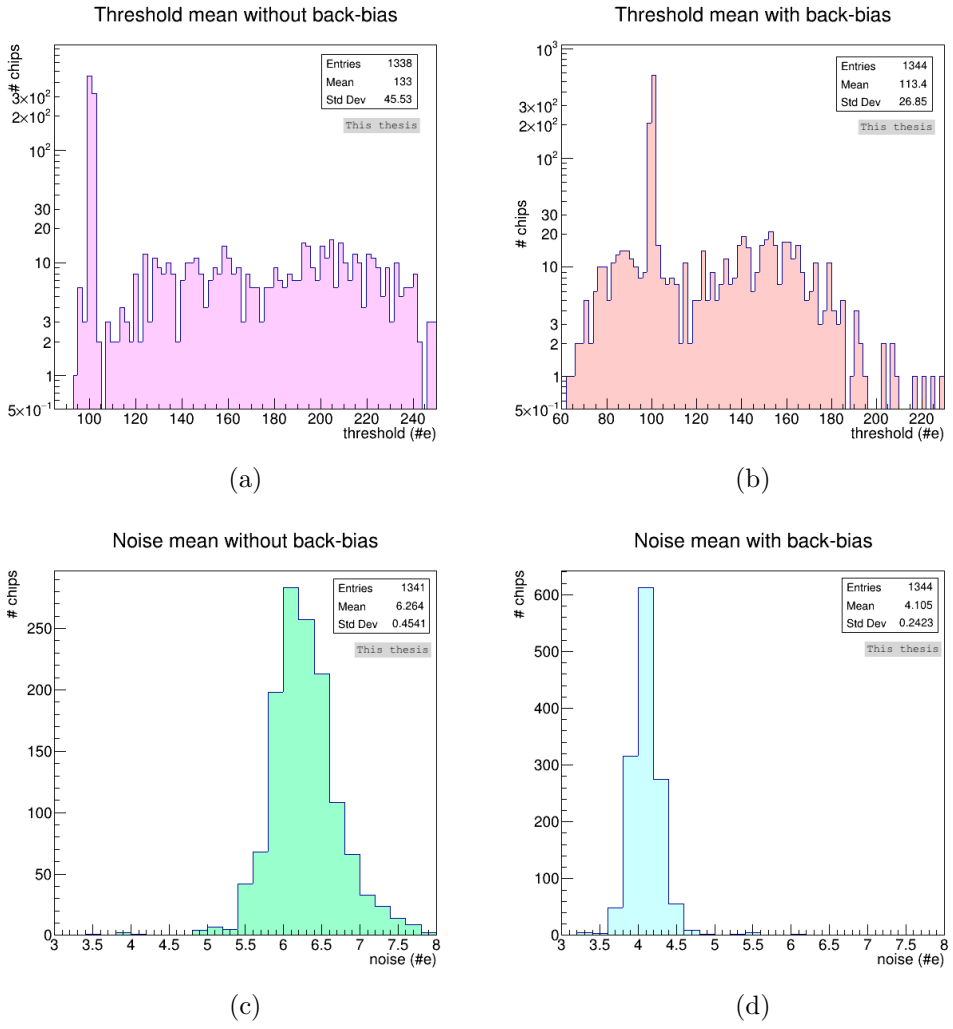

Fig. 4.12: Statistics on threshold and noise values: threshold mean without back-bias (a), threshold mean with back-bias (b), noise mean without back-bias (c), noise mean with back-bias (d).

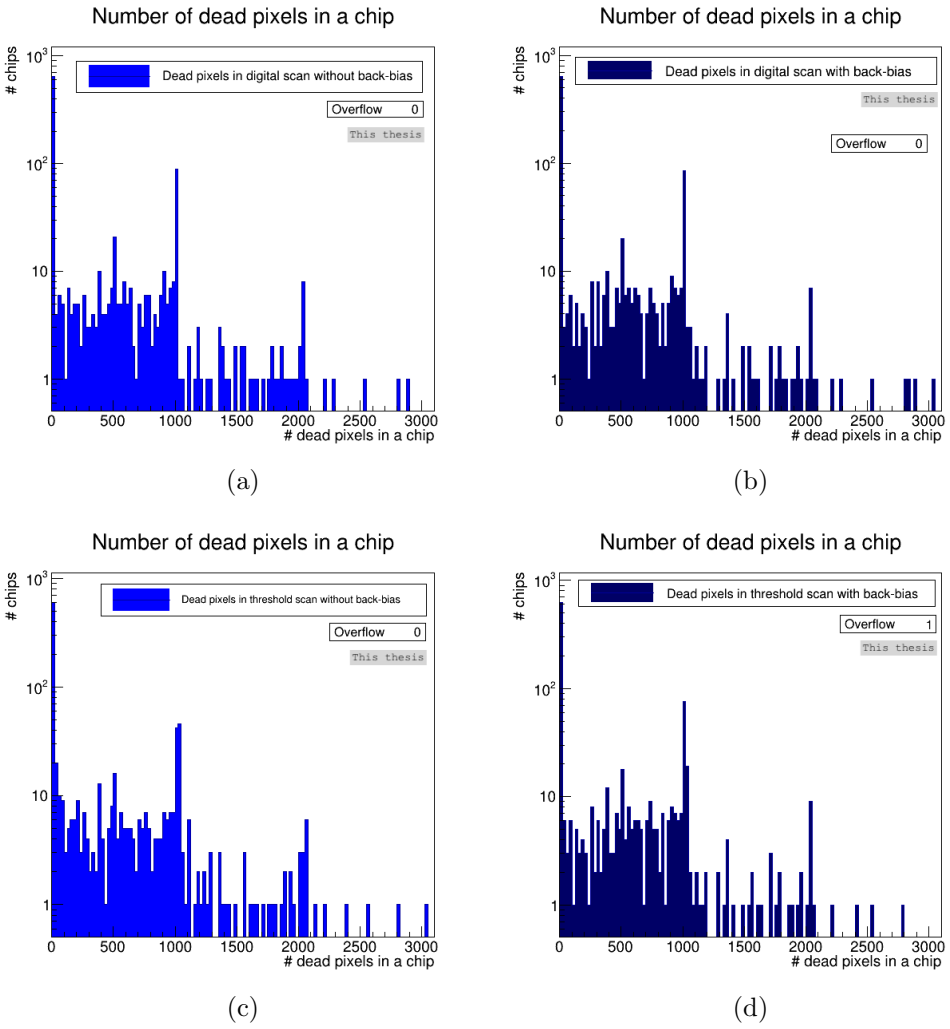

Fig. 4.13: Number of dead pixels per chip in digital scan with $V_{\mathrm{BB}} = 0$ V (a) and with $V_{\mathrm{BB}} = -3$ V (b). Number of dead pixels per chip in threshold scan with $V_{\mathrm{BB}} = 0$ V (c) and with $V_{\mathrm{BB}} = -3$ V (d).

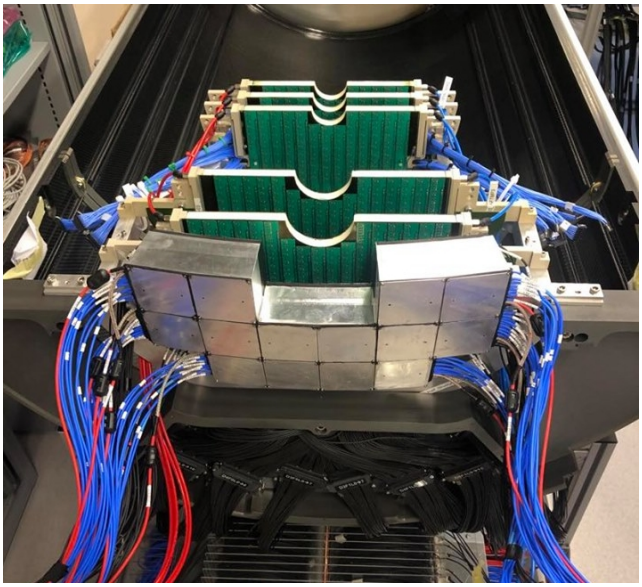

Fig. 4.14: The MFT half-cone assembled inside the barrel. The picture also show cables, cooling tubes and a part of the Fast Interaction Trigger (T0C+).

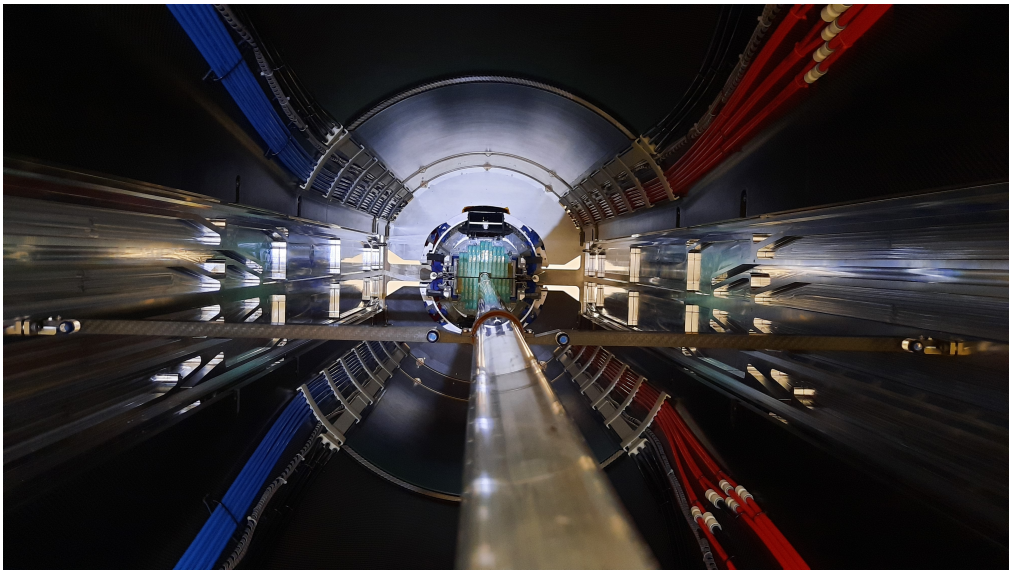

Fig. 4.15: Fully assembled MFT integrated with FIT inside the barrel with the beam pipe in the center [47].

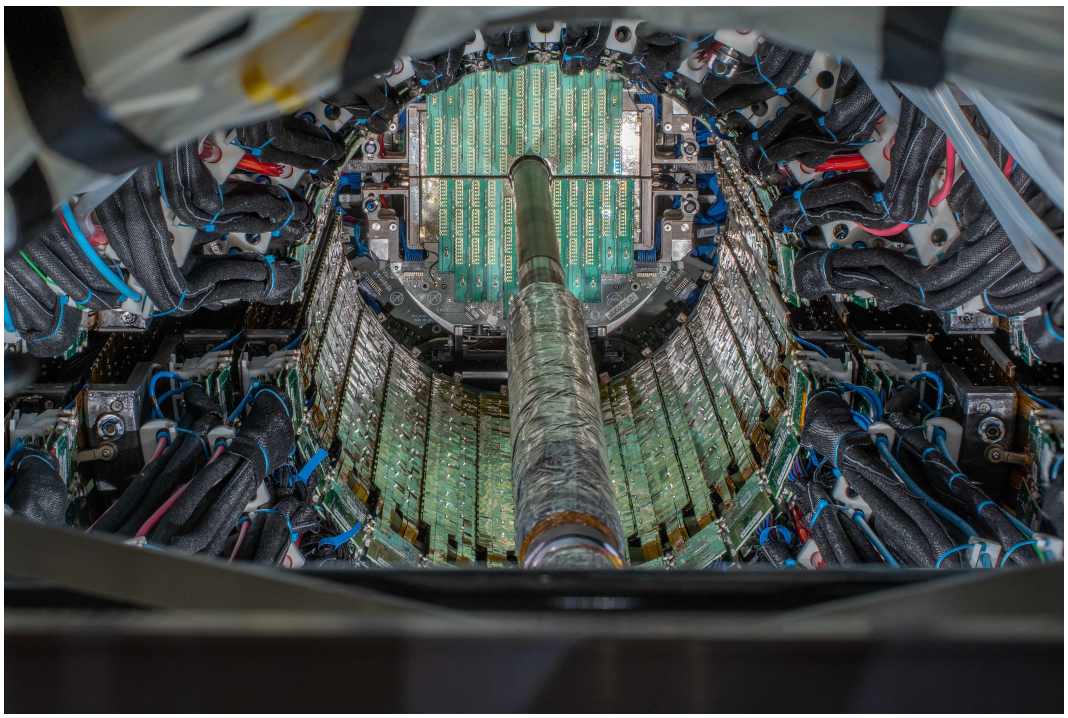

Fig. 4.16: MFT with beam pipe and the ITS Outer Barrel installed in the ALICE cavern [48].

Chapter 5

MFT tracking performance for ρ meson photoproduction

Looking at an event in a particle collider, we can identify individual tracks with particles and measure their properties. In an LHC event, thousands of particles per 25 ns bunch crossing can be created and identified.

Measuring various properties of tracks provides valuable information about the created particles [49]. For instance, the particle momentum, measured by the track curvature in a given magnetic field, can be used to reconstruct invariant masses. The origin of the particles is explored by studying the vertices and identifying decays. For short-lived weakly decaying particles, topology can be used for identifying the vertices.

There are two main tasks in tracking: track identification, i.e., associating a set of points to a track; and track fitting to estimate the trajectory parameters. Both steps require the track model, knowledge of the measurement uncertainties and knowledge of the amount of material traversed, to account for energy loss and multiple scattering. Vertexing requires the same two steps: identifying which tracks belong to the same vertex and estimating the vertex properties.

This chapter includes a description of the methods used for tracking in the MFT and results of the study of the MFT prospects for the measurement of ρ meson coherent photoproduction: a potential new field of research for the MFT as standalone detector is explored.

5.1 MFT tracking

The track finding in MFT has to deal with a high density of clusters, coming both from the charged particles produced in heavy-ion collisions and from background particles. Fake clusters produced by the pixel electronic noise above the threshold have to be accounted for too.

For detector multi-layer systems in general, such as ALICE, it is important to determine the ability to distinguish two nearby trajectories (two-track resolution), momentum resolution or impact parameter resolution, often called the distance of closest approach (DCA).

5.1.1 MFT standalone tracking

In MFT, the following forward coordinate system and track model is used:

the state vector is denoted in the following coordinate system:

$$\vec{s} = (x, y, \phi, \tan\lambda, q/p_t)\,, \tag{5.1}$$

where x, y denote position, ϕ is the azimuthal angle and θ is the complementary polar angle $\lambda = \frac{\pi}{2} - \theta_{\text{Polar}}$, see illustration in Fig. 5.1.

A helix track model with the propagation parameter z is used

$$\begin{bmatrix} x \\ y \\ z \end{bmatrix} = \begin{bmatrix} x_0 - \frac{H_z}{(q/p_{t0})k}\sin(\phi_0)\cos(\theta) + \frac{H_z}{(q/p_{t0})k}\sin(\phi_0) + \frac{\cos(\phi_0)}{(q/p_{t0})k}\sin(\theta) \\ y_0 + \frac{H_z}{(q/p_{t0})k}\cos(\phi_0)\cos(\theta) - \frac{H_z}{(q/p_{i0})k}\cos(\phi_0) + \frac{\sin(\phi_0)}{(q/p_{i0})k}\sin(\theta) \\ \Delta z + z_0 \end{bmatrix},$$

where $k = 0.3\,|B_z|$, $H_z = \frac{B_z}{|B_z|}$ and $\theta = -\frac{(q/p_{t0})\Delta z k}{\tan\lambda_0}$.

5.1.2 MFT standalone tracking workflow

The track reconstruction for the charged particles passing through the MFT is done in two steps:

1. Track finding: clusters identified in the sensitive volumes are grouped into track candidates according to chosen criteria. Two algorithms are used for the MFT standalone track finding: linear track finding (LTF) and cellular automaton (CA). The order of LTF and CA is hard-coded in O^2: the LTF algorithm is applied first, the clusters assigned to a track are marked and not used for other tracks. When the LTF cannot find anymore tracks, the CA algorithm is then applied to the remaining clusters. For each found track, a list of associated clusters is stored.

2. Track fitting with a Kalman filter: the track seed is taken as the last cluster position, the p_T from a fast circle fit, η and ϕ from the first and the last track clusters. After that, the Kalman filter update is performed, where the clusters are incorporated to the track and the track parameters are updated. This process is not affected by the track finding method.

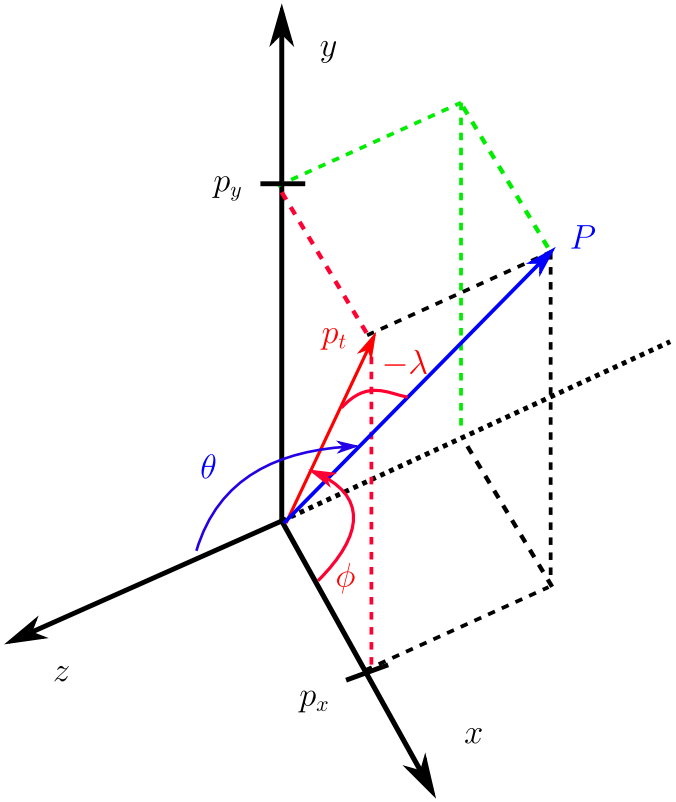

Fig. 5.1: Coordinate system used for MFT tracking.

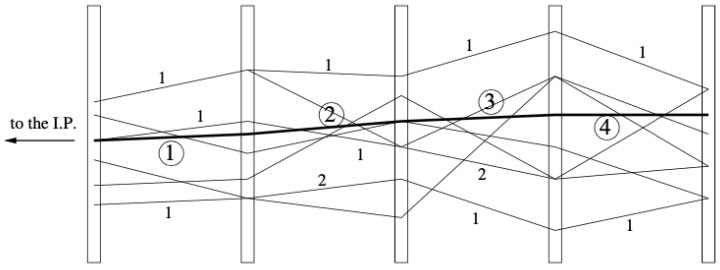

Fig. 5.2: The Cellular Automaton algorithm, where a track is a continuous chain of neighbouring cells with segments connecting clusters in consecutive disks. The cell with status 4 indicates that a track candidate with a length of four segments starts there. Taken from [20].

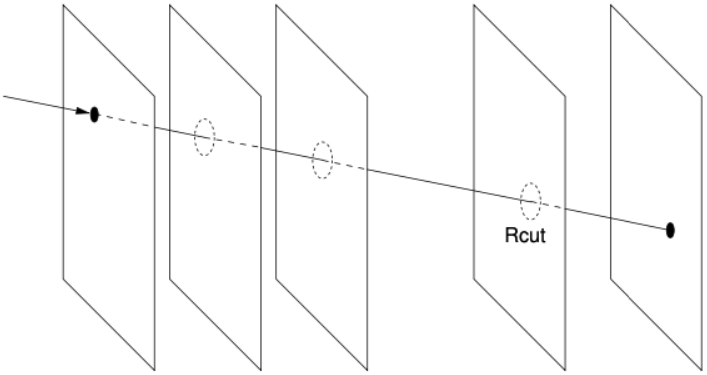

Fig. 5.3: LTF algorithm: an association of one cluster to a track seed, where R_{cut} represents the search radius. Taken from [20].

CA algorithm

In a CA approach, the detector clusters are paired in small units called cells. A cell is defined as a segment connecting two clusters from two consecutive disks of the MFT, see Fig. 5.2. The cells must point to the primary vertex within some angular limits.

The CA begins by considering one given cell. Starting from the first MFT disk, the algorithm proceeds in the direction of propagation of the particles from one MFT disk to the next. Conditions of track continuity are applied in terms of the breaking angle between cells. The cell status, initially at one, increases by one each time another compatible cell is attached to its end.

The CA algorithm, including the mentioned combinatorial procedure, makes the track finding relatively slow for higher multiplicities.

LTF algorithm

The LTF algorithm represents a plain search for straight-line aligned clusters on the MFT planes, starting from a seed connecting two clusters from the outer planes, see Fig. 5.3. The hypothesis assumed is that due to the small radial extension of the MFT and its forward kinematic coverage, the curvature introduced on the tracks by the ALICE solenoid magnet can be neglected.

The LTF track finding process is significantly faster but less efficient in finding tracks at low p_T.

The optimal performance for both the muon physics and for the measurement of global event properties like the charged particle multiplicity in the MFT acceptance is ensured by this hybrid track finding procedure.

5.1.3 MFT standalone track parameters

Track parameters are stored at the cluster closest to the IP. There is a built-in method to propagate to any position and a helix track model valid near the center of the ALICE detector, checked between the last MFT plane and the IP.

The χ^2 of each track is the sum of χ^2's of each Kalman update, executed $(n_{\text{clusters}} - 1)$ times. The value is evaluated during each Kalman update step, the number of track parameters (5) is used as the number of degrees of freedom (DOF).

5.1.4 Kalman filtering

The Kalman filter [50] is a recursive procedure for estimating the state parameters of a linear discrete dynamic system (e.g. a track in a particle physics detector). An essential ingredient in the Kalman technique is the covariance matrix of the track parameters due to multiple Coulomb scattering. The Kalman filtering method represents a general method for evaluating the covariance matrices.

Calculation of covariance matrices

Multiple scattering is conveniently parameterised by two mutually orthogonal, uncorrelated scattering angles θ_1 and θ_2, which are assumed to be small. The coveriance matrix elements $\langle \theta_i, \theta_j \rangle$ for the scattering angles θ_1 and θ_2 can be written as

$$\langle \theta_i, \theta_j \rangle = \sigma^2 \left(\theta_{proj} \right) \delta_{ij}, \tag{5.2}$$

where $\sigma^2 \left(\theta_{proj} \right)$ is the variance of the projected multiple scattering angle. The covariance matrix elements $\langle P_i, P_j \rangle$ for any two arbitrary functions can be evaluated using the propagation of errors formula and substituting into Eq. (5.2)

$$\langle P_i, P_j \rangle = \sum_{m,n=1}^{2} \frac{\partial P_i}{\partial \theta_m} \frac{\partial P_j}{\partial \theta_n} \langle \theta_m, \theta_n \rangle \tag{5.3}$$

$$= \sigma^2 \left(\theta_{\text{proj}} \right) \left(\frac{\partial P_i}{\partial \theta_1} \frac{\partial P_j}{\partial \theta_1} + \frac{\partial P_i}{\partial \theta_2} \frac{\partial P_j}{\partial \theta_2} \right) \tag{5.4}$$

Hence, the evaluation of the partial derivatives of the track parameters with respect to the two orthogonal scattering angles is required for the calculation of the covariance matrix elements.

5.1.5 Vertex position estimation: reducing the combinatorics

In ALICE, a precise measurement of the interaction vertex is provided by the ITS. The MFT could, however, still be able to provide a standalone rough estimation of the primary vertex position, which could significantly reduce the computing time when building cells and seeds in the CA and LTF methods. This is possible by building the cells between the first two disks of the detector, then extrapolating them to the beam axis to compute the closest approach z-position: the peak corresponding to cells produced by the primary tracks is well distinguishable from the combinatorial cells background. This method, allowing to identify the z-vertex position with a RMS ~ 2 mm, is only achievable in a very high multiplicity event, expected with centrality close to 50% in Pb–Pb collisions at $\sqrt{s_{\mathrm{NN}}} = 5.5$ TeV.

5.2 MFT perspective for the measurement of ρ meson photoproduction in Run 3

This topic has been studied as a potential new physics topic for the MFT as a stand-alone detector. The STARlight [37] event generator in O^2 was used, studying the decay channel $\rho^0 \to \pi^+\pi^-$. A total of 500 000 Pb–Pb events with the interaction rate set to 50 kHz were used. A standard MFT reconstruction workflow was used: MFT digits were grouped in MFT clusters using the dictionary of cluster topologies. A ROF (read-out frame) is a container for standalone track fitting; in time units, its length can be expressed as 96 bunch crossings (BC), corresponding to 9880.51 ns. The tracker module subsequently processes ROFs, finds tracks (see Sec. 5.1.2) using LTF and CA methods and the track fitting is performed using a Kalman filter with parameters updated by computing each cluster using Kalman steps. As there is no available framework to find the reconstructed vertex yet, the MC generated one was used for the track propagation: each track was propagated to the generated z coordinate at the origin of the particle as given by the MC generator. After the reconstruction, MFT tracks were matched with the corresponding MC tracks. For this study, we used only ROFs with 2 MFT tracks: out of 500 000 MC events used, 173 326 such ROFs were found.

5.2.1 Standalone MFT tracks

In Fig. 5.4, the p_T distribution was plotted separately for MC and reconstructed MFT tracks.

The distribution of the number of clusters per track is in Fig. 5.5. Such histogram separately for CA and LTF tracks, is used in the QC Track task,

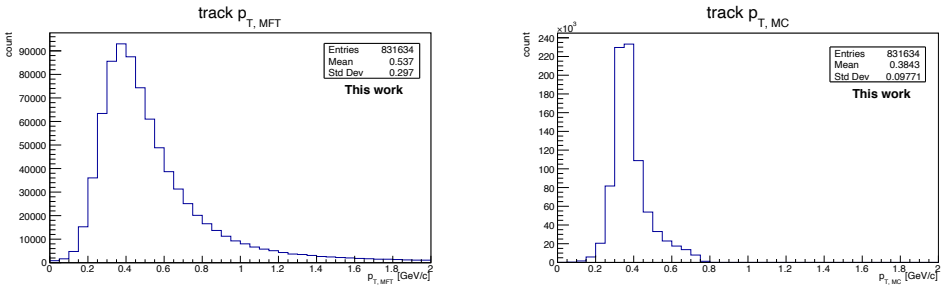

(a) (b)

Fig. 5.4: Transverse momentum distributions of standalone tracks reconstructed with the MFT and of corresponding MC tracks.

see Sec. 1.3.1. As the LTF algorithm is applied first, only the clusters not used by the LTF algorithm are fed to the CA algorithm. This might create a bias in this study: the LTF algorithm does not find tracks at small η with such efficiency, as can be seen in Fig. 5.6; this might affect the kinematics. It was also observed that in STARlight, the ϕ distribution is inverted and shifted by $\pi/2$ with respect to MFT track ϕ distibution, which also needs to be accounted for.

If we compare p_T distributions for CA and LTF tracks in Fig. 5.7, a worse p_T resolution is observed for LTF tracks, as they represent a straight-line with no curvature.

5.2.2 Track pairs

Out of the mentioned 173 326 ROFs with two tracks, a large majority (almost 99%) is represented by the LTF+LTF pairs. For the mixed type CA+LTF, there are 1920 cases and for CA+CA pairs: only 32 such pairs were present. Correlation plots of the track pair m and p_T on MC and MFT level is in Fig. 5.8.

For LTF+LTF pairs, tails are observed in the p_T and m distributions in Fig. 5.9, whereas in the mixed CA+LTF pairs, we obtain significantly better resolution yet lower statistics. These properties were used to further study MFT resolution: a further look at ρ mesons reconstructed from CA+LTF pairs can be found in Fig. 5.10 and 5.11.

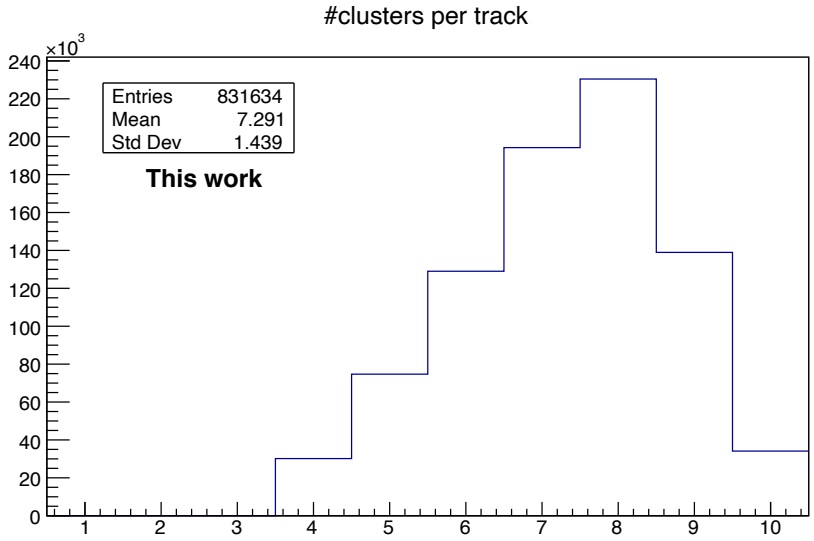

Fig. 5.5: Number of clusters per MFT track for both CA and LTF tracks.

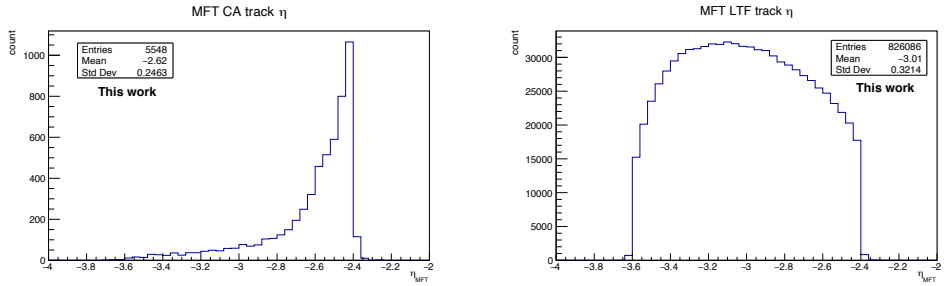

(a) (b)

Fig. 5.6: Pseudorapidity η distributions for CA and LTF tracks.

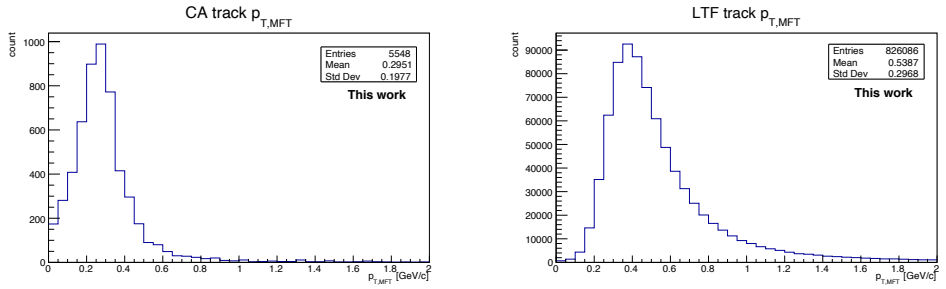

(a) (b)

Fig. 5.7: Transverse momentum p_T distributions for CA and LTF tracks.

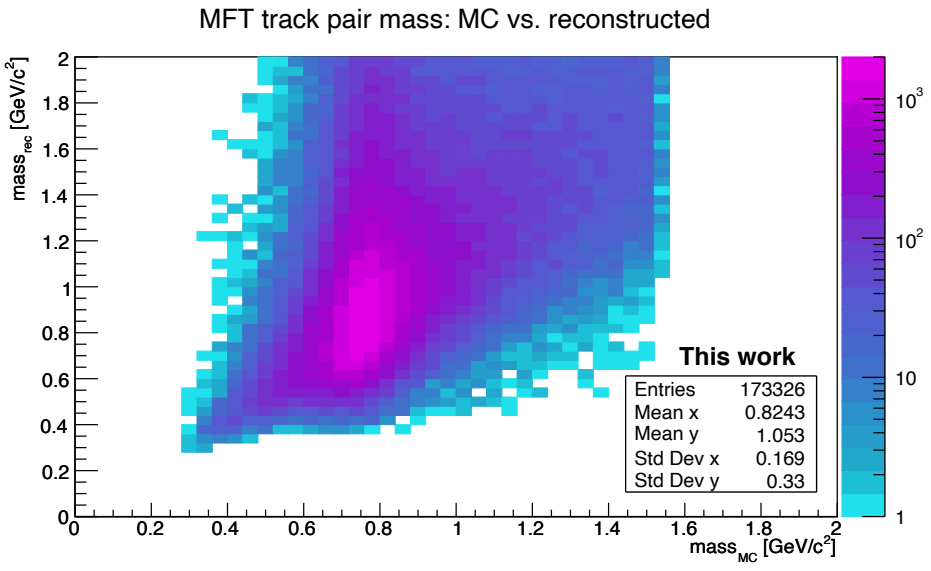

(a)

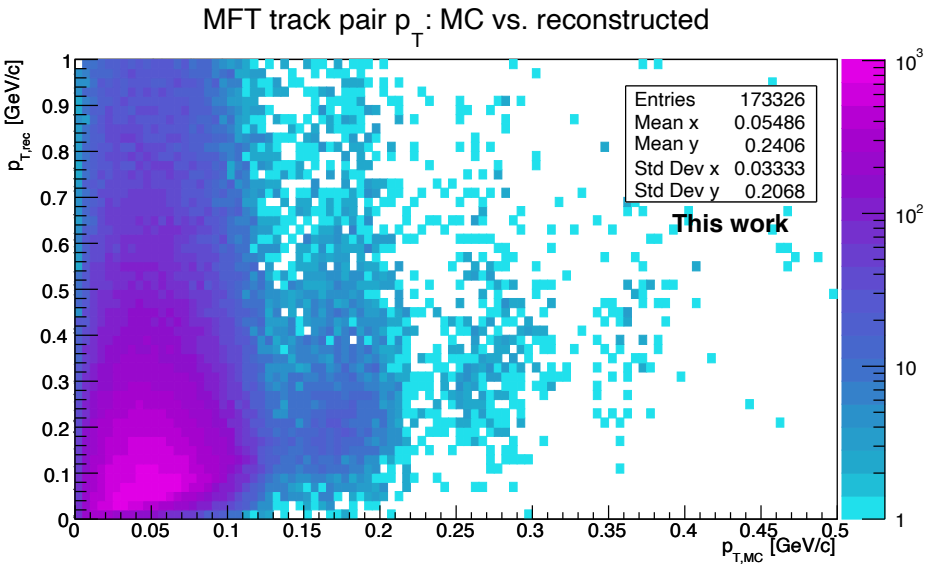

(b)

Fig. 5.8: Invariant mass and p_T distributions of ρ mesons reconstructed from track pairs.

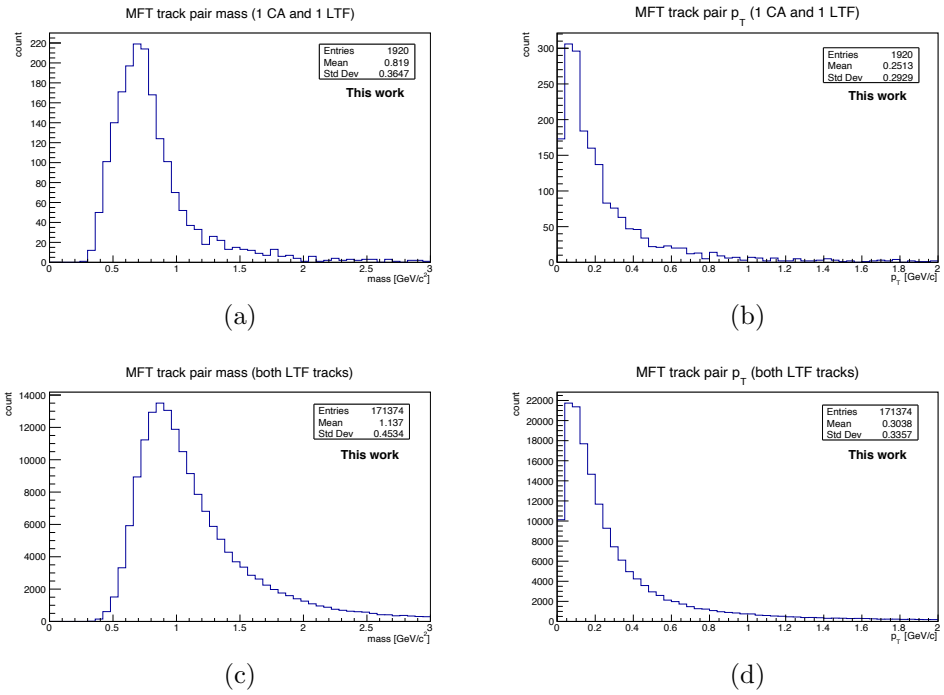

Fig. 5.9: Mass and transverse momentum p_T distributions for the ρ meson reconstructed from CA+LTF and LTF+LTF track pairs.

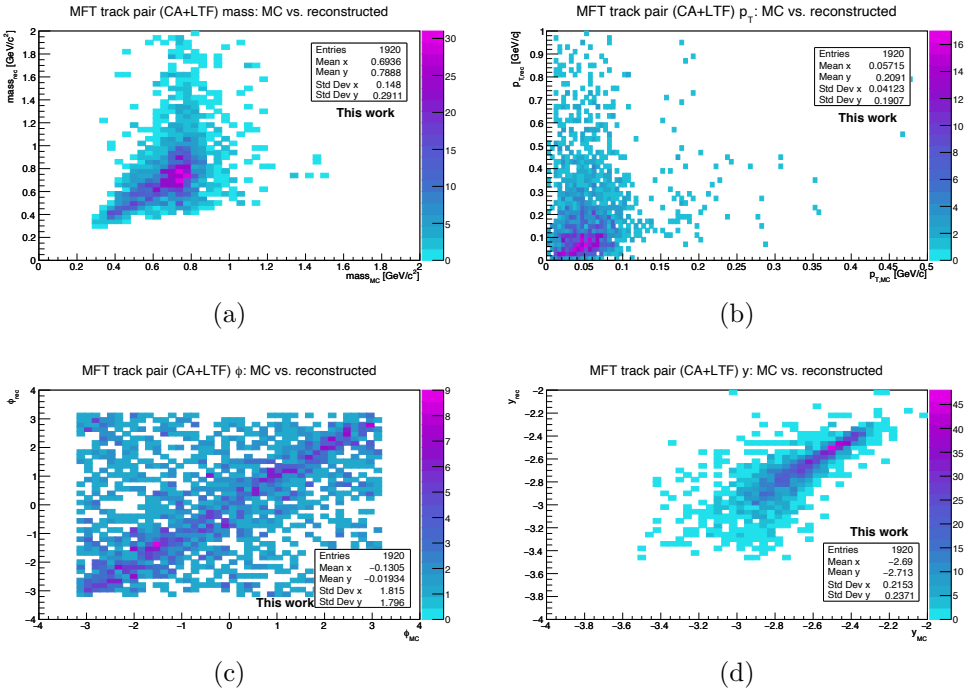

(a) (b)

(c) (d)

Fig. 5.10: m, p_T, ϕ and y distributions for the ρ meson reconstructed from CA+LTF pairs.

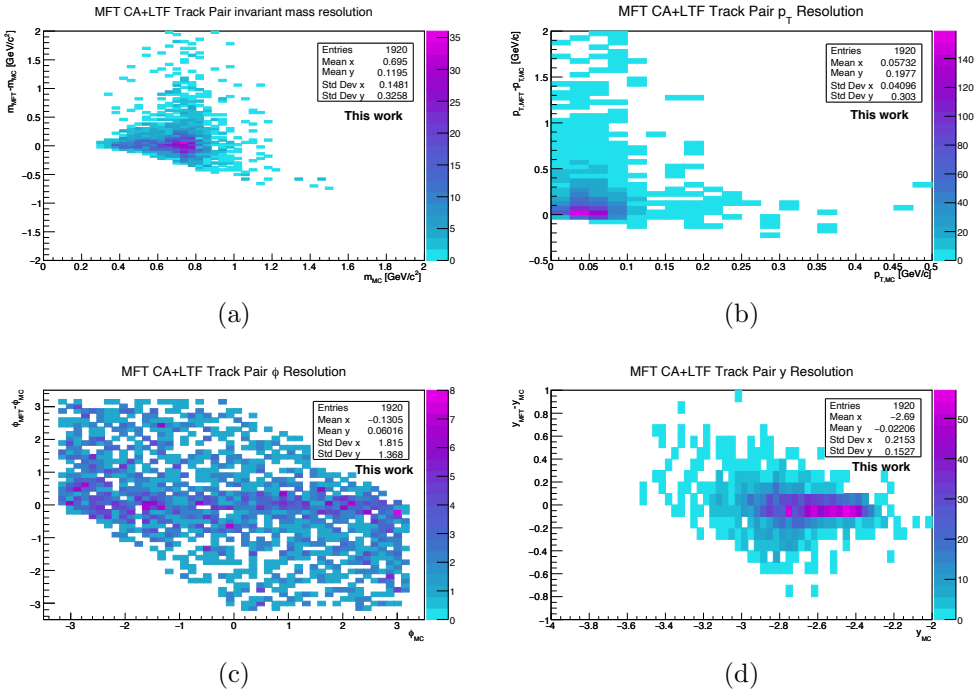

(a) (b)

(c) (d)

Fig. 5.11: Resolutions in m, p_T, ϕ, η for CA+LTF pairs.

5.2.3 CA track pairs

A sample of 50 000 STARlight events was reconstructed with the CA algorithm only. Resolutions for the obtained 13 562 CA+CA track pairs are shown in Fig. 5.12. In this case, around 27% of the tracks pairs were CA+CA which has significantly better resolution, as shown in Fig. 5.9. When compared to the standard reconstruction, only 0.4% LTF+CA or CA+CA pairs were found, and approximately 34% of the track pairs are LTF+LTF, which have the worst resolution.

5.2.4 Conclusions

This study was performed to quantify the performance of the MFT as a standalone detector, as there is no available framework to match the tracks with the ALICE muon spectrometer or to reconstruct the vertices yet. Both mentioned tools are currently under development.

The performance of the two different tracking algorithms used in the MFT was studied. A significantly better performance was observed for CA+LTF pairs: although smaller statistics is provided, the analysis of ρ photoproduction using the MFT should be feasible given the expected number of ρ mesons in Run 3 (see Tab. 3.1). The study of the performance could be extended to

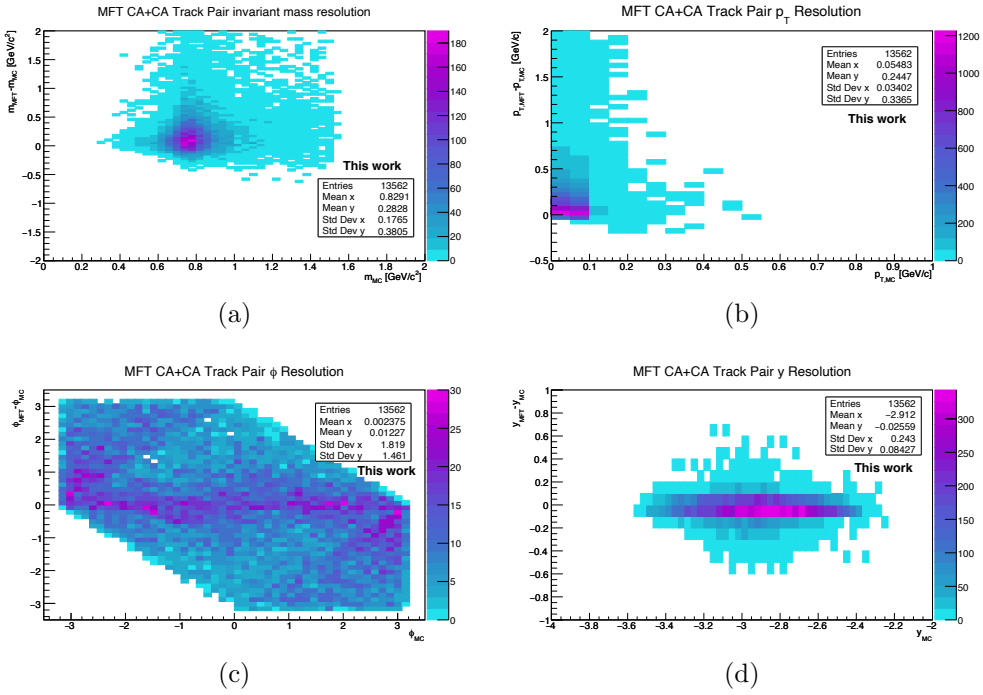

(a) (b)

(c) (d)

Fig. 5.12: Resolutions in m, p_T, ϕ, η for CA+CA pairs.

evaluate the dependence on the number of clusters or the χ^2 values of the track fit. More detailed studies will be conducted in that direction to further quantify the performance.

Chapter 6

Summary and outlook

releasing,
learning,
expanding–
i am happily a
work in progress

Yung Pueblo: Inward [51]

The Run 3 at the LHC will be performed at a significantly higher luminosity, therefore the ALICE upgrade project consists of numerous improvements. Besides the upgraded hardware, including the new gas electron multipliers in the TPC, the silicon ALPIDE chips in both ITS and the MFT, or the FIT detector, the data processing will also undergo a major change: from the trigger mode to continuous processing in a framework called O^2. This will allow us to perform new measurements with even higher accuracy.

This work was devoted to the performance study of the MFT, a new detector which was designed to allow precise vertexing capabilities to muon tracking at forward rapidity in ALICE.

To clarify the basic motivation to add the forward tracking detector to the ALICE detector system, the current state of the experiment and upgrade plans were presented in Chapter 1. The layout of the MFT, consisting of 10 half-disks with 2 detection planes each, is also presented here.

A description of silicon detectors in general with an emphasis on ALPIDE sensors used for both the ITS and the MFT after the upgrade was presented in Chapter 2.

The physics motivation for the MFT was described in Chapter 3. Prospects for the study of heavy flavours and charmonia were presented, along with an introduction to ultra-peripheral collisions and recent measurements.

The technical part of the work that I participated in at CERN was presented in Chapter 4, where the specific procedures of the MFT commissioning

were described. The statistical analysis of the qualification results was also summarised here.

Methods used for tracking in MFT along with the results of studies of ρ meson photoproduction, representing a potential use of the MFT as standalone detector, were presented in Chapter 5. This part of the work contributes to the study of the MFT performance and for the development of quality control system of the detector.

After the MFT tests on surface and installation in ALICE cavern in December 2020, the commissioning continues. The quality control development and calibration are ongoing. According to the current LHC schedule, we are expecting the first test beams in September 2021. In May 2022, after the global commissioning and calibration will be done, the first LHC beams in Run 3 are expected to be measured to bring exciting new physics discoveries.

Long-term outlook

After the next LHC shutdown in 2025, the ALICE detector system in Run 4 will include FoCal, the system of forward electromagnetic and hadronic calorimeters and the ITS3 with the three innermost layers replaced. The interest to continue to improve the central silicon tracking detector in ALICE has been expressed in [52, 53]. The ITS3 would be a novel vertex detector consisting of wafer-scale ultrathin MAPS in curved, perfectly cylindrical layers. The control logic, data buffers, and links would be placed at the edge of the sensor. According to ALICE upgrade simulations, the ITS3 will result in reduced combinatorial background, better charm rejection access to the most sensitive region for coalescence, or better resolution of the (anti-)deuteron impact parameter crucial to discriminate the signal from background.

Concerning ALICE in the LHC Run 5 [54], as mentioned in the Update of the European strategy for particle physics [55], the ambition is to *design a new experiment to continue with a rich heavy-ion programme at the HL-LHC*. The goal for ALICE is to study pp, pA, and AA collisions at luminosities 20-50$\times$ higher that in ALICE in Runs 3-4. What was presented would be a compact, all-silicon *nearly massless* detector with excellent low-p_T tracking capabilities. The innermost layers would be placed possibly inside the beam pipe.

The silicon detectors in general will clearly play an important role in the future of HEP. The work at the MFT, which is a prominent example of where the current silicon technology stands, is a great experience for me as a particle physicist to use the acquired knowledge and, by learning how to detect the elementary particles, allows me to acquire deeper understanding of what the particles actually represent.

Prague, April 2021

Bibliography

[1] Marcus Chown. Twitter. 2009. URL: https://twitter.com/marcuschown/status/3914162203.

[2] Douglas Adams. *The Salmon of Doubt*. London: Pan Macmillan, 2012.

[3] Francesco Noferini on behalf of the ALICE Collaboration. *ALICE results from Run-1 and Run-2 and perspectives for Run-3 and Run-4*. 2018.

[4] *LHC long term schedule*. URL: https://lhc-commissioning.web.cern.ch/schedule/LHC-long-term.htm.

[5] C. Fabjan and J. Schukraft. *The story of ALICE: Building the dedicated heavy ion detector at LHC*. 2011. eprint: arXiv:1101.1257.

[6] Arturo Tauro. "ALICE Schematics". General Photo. 2017. URL: https://cds.cern.ch/record/2263642.

[7] K. Aamodt et al. "The ALICE experiment at the CERN LHC". In: *JINST* 3 (2008), S08002. DOI: 10.1088/1748-0221/3/08/S08002.

[8] ALICE Collaboration. "Performance of the ALICE Experiment at the CERN LHC". In: *Int. J. Mod. Phys. A 29 (2014) 1430044* (2014). DOI: 10.1142/S0217751X14300440. eprint: arXiv:1402.4476.

[9] B Abelev et al. *Technical Design Report for the Upgrade of the ALICE Inner Tracking System*. Tech. rep. CERN-LHCC-2013-024. ALICE-TDR-017. 2013. DOI: 10.1088/0954-3899/41/8/087002. URL: https://cds.cern.ch/record/1625842.

[10] J. Alme et al. "The ALICE TPC, a large 3-dimensional tracking device with fast readout for ultra-high multiplicity events". In: *Nucl.Instrum.Meth.A622:316-367,2010* (2010). DOI: 10.1016/j.nima.2010.04.042. eprint: arXiv:1001.1950.

[11] ALICE Collaboration. "The ALICE Transition Radiation Detector: construction, operation, and performance". In: *Nucl. Instrum. Meth. A 881 (2018) 88* (2017). DOI: 10.1016/j.nima.2017.09.028. eprint: arXiv:1709.02743.

[12] ALICE Collaboration. *The ALICE Dimuon Spectrometer*. 2008. URL: http://aliceinfo.cern.ch/Public/en/Chapter2/Chap2_dim_spec.html.

[13] *ALICE dimuon forward spectrometer: addendum to the Technical Design Report*. Technical Design Report ALICE. Geneva: CERN, 2000. URL: https://cds.cern.ch/record/494265.

[14] M Gallio et al. *ALICE Zero-Degree Calorimeter (ZDC): Technical Design Report*. Technical Design Report ALICE. Geneva: CERN, 1999. URL: https://cds.cern.ch/record/381433.

[15] ALICE Collaboration. "Performance of the ALICE VZERO system". In: (2013). DOI: 10.1088/1748-0221/8/10/P10016. eprint: arXiv:1306.3130.

[16] ALICE Collboration. *ALICE Schematics as during RUN3 (after upgrade)*. ALICE-PHO-SKE-2017-001-5. 2017.

[17] B Abelev et al. "Upgrade of the ALICE Experiment: Letter Of Intent". In: *J. Phys.* G41 (2014), p. 087001. DOI: 10.1088/0954-3899/41/8/087001.

[18] P Buncic, M Krzewicki, and P Vande Vyvre. *Technical Design Report for the Upgrade of the Online-Offline Computing System*. Tech. rep. CERN-LHCC-2015-006. ALICE-TDR-019. 2015. URL: https://cds.cern.ch/record/2011297.

[19] *Addendum of the Letter of Intent for the upgrade of the ALICE experiment : The Muon Forward Tracker*. Tech. rep. CERN-LHCC-2013-014. LHCC-I-022-ADD-1. Geneva: CERN, 2013. URL: https://cds.cern.ch/record/1592659.

[20] *Technical Design Report for the Muon Forward Tracker*. Tech. rep. CERN-LHCC-2015-001. ALICE-TDR-018. 2015. URL: https://cds.cern.ch/record/1981898.

[21] Diana Mária Krupová. *Commissioning of the Muon Forward Tracker for ALICE upgrade*. Research project. Sept. 2020. URL: https://indico.fjfi.cvut.cz/event/135/contributions/2794/attachments/921/1257/VU_DK.pdf.

[22] Angelo Rivetti. *CMOS Front-End Electronics for Radiation Sensors*. CRC Press, 2015. ISBN: 978-1-4665-6310.

[23] Gianluca Aglieri Rinella. *Overview of the ALPIDE Pixel Sensor Chip with focus on Readout Features*. 2017. URL: https://indico.cern.ch/event/666016/contributions/2722251/attachments/1523408/2380925/20170914-ALPIDE-FoCal-Study-Aglieri.pdf.

[24] Lucrezia Camilla Migliorin. *Évaluation expérimentale de la performance du détecteur MFT développé pour les Runs 3 et 4 du LHC*. Tech. rep. Université Claude Bernard Lyon 1, 2019.

[25] Przemyslav Karczmarczyk. *Characterization of the pAlpide chip for the Muon Forward Tracker detector*. Tech. rep. Warsaw University of Technology, 2016.

[26] Cesar Augusto Marin Tobon. "PADRE pixel read-out architecture for Monolithic Active Pixel Sensor for the new ALICE Inner Tracking System in TowerJazz 180 nm technolog". presented 19 Jul 2017. 2017. DOI: 10251/86154. URL: https://cds.cern.ch/record/2316141.

[27] Z. Citron et al. *Future physics opportunities for high-density QCD at the LHC with heavy-ion and proton beams*. 2018. eprint: arXiv:1812.06772.

[28] "ALICE upgrade physics performance studies for 2018 Report on HL/HE-LHC physics". In: (2019). URL: https://cds.cern.ch/record/2661798.

[29] M. Tanabashi et al. "Review of Particle Physics". In: *Phys. Rev. D* 98 (3 2018), p. 030001. DOI: 10.1103/PhysRevD.98.030001. URL: https://link.aps.org/doi/10.1103/PhysRevD.98.030001.

[30] Michael L. Miller et al. "Glauber Modeling in High Energy Nuclear Collisions". In: *Ann.Rev.Nucl.Part.Sci.57:205-243,2007* (2007). DOI: 10.1146/annurev.nucl.57.090506.123020. eprint: arXiv:nucl-ex/0701025.

[31] Javier Castillo. "Measurements of quarkonium production with ALICE at the LHC". In: *Journal of Physics G: Nuclear and Particle Physics* 37.9 (Sept. 2010), p. 94051. DOI: 10.1088/0954-3899/37/9/094051. URL: https://hal.archives-ouvertes.fr/hal-00600858.

[32] Louis Kluberg and Helmut Satz. *Color Deconfinement and Charmonium Production in Nuclear Collisions*. 2009. DOI: 10.1007/978-3-642-01539-7_13. eprint: arXiv:0901.3831.

[33] Antonio Uras. *Muon Physics in ALICE: The MFT Upgrade Project*. 2012. DOI: 10.1088/1742-6596/446/1/012054. eprint: arXiv:1212.6517.

[34] Antonio Uras. *The ALICE MFT Project: Motivations and Expectations*. 2012. URL: http://llr.in2p3.fr/sites/qgp2012/Talks/Etretat_2012_Uras2.pdf.

[35] J. G. Contreras and J. D. Tapia Takaki. "Ultra-peripheral heavy-ion collisions at the LHC". In: *Int. J. Mod. Phys., A30:1542012* (2015).

[36] Gerhard Baur et al. "Coherent gamma-gamma and gamma-A interactions in very peripheral collisions at relativistic ion colliders". In: (2001). DOI: 10.1016/S0370-1573(01)00101-6. eprint: arXiv:hep-ph/0112211.

[37] Spencer R. Klein et al. "STARlight: A Monte Carlo simulation program for ultra-peripheral collisions of relativistic ions". In: *Comput.Phys.Commun. 212 (2017) 258-268* (2016). DOI: 10.1016/j.cpc.2016.10.016. eprint: arXiv:1607.03838.

[38] ALICE Collaboration. "Coherent ^{0} photoproduction in ultra-peripheral Pb-Pb collisions at $\sqrt{s_{\mathrm{NN}}} = 2.76$ TeV". In: *JHEP 09 (2015) 095* (2015). DOI: 10.1007/JHEP09(2015)095. eprint: arXiv:1503.09177.

[39] ALICE Collaboration. "Coherent photoproduction of ρ^0 vector mesons in ultra-peripheral Pb-Pb collisions at $\sqrt{\mathrm{s_{NN}}} = 5.02$ TeV. Coherent photoproduction of ρ^0 vector mesons in ultra-peripheral Pb–Pb collisions at $\sqrt{s_{NN}} = 5.02$ TeV". In: *JHEP* 2006.arXiv:2002.10897 (2020). Figures at http://alice-publications.web.cern.ch/node/6147, 035. 28 p. DOI: 10.1007/JHEP06(2020)035. URL: https://cds.cern.ch/record/2710371.

[40] ALICE Collaboration. *First measurement of coherent ^{0} photoproduction in ultra-peripheral Xe-Xe collisions at $\sqrt{\mathbf{s_{NN}}} = \mathbf{5.44}$ TeV*. 2021. eprint: arXiv:2101.02581.

[41] *LHC long term schedule*. online, accessed March 14, 2021. URL: https://lhc-commissioning.web.cern.ch/schedule/LHC-long-term.htm.

[42] G De Robertis et al. "A MOdular System for Acquisition, Interface and Control (MOSAIC) of detectors and their related electronics for high energy physics experiment". In: *EPJ Web Conf.* 174 (2018), 07002. 4 p. DOI: 10.1051/epjconf/201817407002. URL: https://cds.cern.ch/record/2314957.

[43] Lukas Arts. "ALPIDE Testing Software for the upgraded Inner Tracking System of the ALICE experiment". 2016. URL: https://dspace.library.uu.nl/handle/1874/330984.

[44] P. Yang et al. "Low-power priority Address-Encoder and Reset-Decoder data-driven readout for Monolithic Active Pixel Sensors for tracker system". In: *Nuclear Instruments and Methods in Physics Research Section A Accelerators Spectrometers Detectors and Associated Equipment* 785 (June 2015), pp. 61–69. DOI: 10.1016/j.nima.2015.02.063.

[45] *Eye diagrams: The tool for serial data analysis - EDN*. https://www.edn.com/eye-diagrams-the-tool-for-serial-data-analysis. (Accessed on 03/14/2021).

[46] ALICE ITS ALPIDE development team. *ALPIDE Operations Manual*. 2016. URL: http://www-subatech.in2p3.fr/~electro/projets/alice/dimuon/mft/pdf/ALPIDE-4-operations-manual_draft20160601.pdf.

[47] MFT Collaboration ALICE. "ALICE Muon Forward Tracker (MFT)". In: (2020). General Photo. URL: https://cds.cern.ch/record/2748310.

[48] Felix Reidt, Jochen Klein, and Marc Alain Imhoff. "ALICE ITS Outer Barrel Installation". General Photo. 2021. URL: https://cds.cern.ch/record/2759554.

[49] Jérôme Baudot. *Tracking*. https://indico.cern.ch/event/782305/contributions/3256039/attachments/1787393/2911880/tracking_ESIPAP.pdf. (Accessed on 03/20/2021). 2019.

[50] E.J Wolin and L.L Ho. "Covariance matrices for track fitting with the Kalman filter". In: *Nuclear Instruments and Methods in Physics Research Section A: Accelerators, Spectrometers, Detectors and Associated Equipment* 329.3 (1993), pp. 493 –500. ISSN: 0168-9002. DOI: https://doi.org/10.1016/0168-9002(93)91285-U. URL: http://www.sciencedirect.com/science/article/pii/016890029391285U.

[51] Yung Pueblo. *Inward*. Kansas City: Andrews McMeel Publishing, 2018.

[52] ALICE Collaboration. *Expression of Interest for an ALICE ITS Upgrade in LS3*. 2018. URL: http://cds.cern.ch/record/2644611.

[53] Luciano Musa. *Letter of Intent for an ALICE ITS Upgrade in LS3*. Tech. rep. CERN-LHCC-2019-018. LHCC-I-034. Geneva: CERN, 2019. URL: https://cds.cern.ch/record/2703140.

[54] Andrea Rossi. *ALICE upgrades for LHC Run 4 and beyond*. 2020. URL: https://indi.to/nGCgm.

[55] *2020 Update of the European Strategy for Particle Physics (Brochure)*. Tech. rep. CERN-ESU-015. Geneva, 2020. URL: https://cds.cern.ch/record/2721370.